

Numerical simulation of bubble deformation and breakup under simple linear shear flows

Mitsuhiro Ohta^{1,1,*}, Tetsuya Ueta¹, Yozo Toei¹, Edwin Jimenez¹, Mark Sussman¹

Abstract

Numerical simulations are presented for the deformation and breakup of a bubble in liquids undergoing simple linear shear flow in a variety of regimes including the low Capillary number, high Reynolds number regime. Numerical results are obtained using a projection method for incompressible two-phase flow. The method represents interfaces using the sharp interface coupled level set and Volume-Of-Fluid (CLSVOF) method. To verify the CLSVOF numerical algorithm and provide a basis for comparison, computational results are also presented that compare with previous, more popular, drop deformation and rupture simulations. The numerical results reveal that the shear-induced bubble deformation and breakup process differs significantly from that of the analogous drop system under similar flow conditions. The first distinguishing factor for bubble breakup is that the magnitude of shear flow necessary for causing rupture is much larger than that in the drop system case. In other words, a larger Reynolds number is needed to induce bubble breakup. The second distinct feature of the bubble system versus the drop system is that the bubble does not maintain a stable deformed shape as the system parameters approach the critical “breakup” Reynolds number. It is asserted that the differences in morphology for a bubble undergoing breakup versus a drop in the same process can be attributed to the density and viscosity ratio of the corresponding two-phase flow systems. The critical conditions for bubble breakup with respect to the Reynolds and capillary numbers are determined for several cases.

Keywords: Bubble deformation, bubble breakup, shear flow, CFD

¹ 1. Introduction

Bubble dynamics in shear flow, including breakup, is critically important for various gas-liquid scientific and engineering processes. We refer the reader to the following experimental studies relating to bubble deformation in foaming processes, microfluidic devices, microbubbles in the blood circulation system,

*Corresponding author: m-ohta@tokushima-u.ac.jp

6 materials processing, pharmaceuticals, minerals engineering, bubble column re-
7 actor, underwater projectiles, polyethylene devolatilization, microfluidics, food
8 aeration, passive cyclonic separators, and cosmetics[7, 36, 4, 11, 12, 67, 13, 71,
9 5, 17, 70, 15, 16, 35, 52, 51, 21, 54]. In particular, it is the study of bubble de-
10 formation as it pertains to high-performance plastics applications that motivate
11 this work.

12 This article presents computational studies of shear-driven deformation and
13 breakup of a bubble in insoluble viscous liquids. Studying bubble break-up,
14 in which we focus only on the balance of the wall driving force and bubble
15 surface tension force, via computation rather than experiments simplifies the
16 process of setting a combination of precise, simple shear flow conditions, low
17 Capillary number ($Ca = \mu_m U / \sigma$) conditions, high Reynolds' number conditions
18 ($Re = \rho_m R U / \mu_m$), low-density ratio, low viscosity ratios, and zero buoyancy ef-
19 fects. We remark that previous controlled experimental studies on shear-driven
20 bubble deformation are restricted to the low Reynolds' number and large capil-
21 lary number regime[50, 5]. One reason is that buoyancy effects are minimized in
22 highly viscous liquids. On the other hand, many applications are characterized
23 by liquids in the high Reynolds' number regime. The physical properties that
24 distinguish bubble and drop studies are expressed in terms of the density ratio
25 $\lambda = \rho_b / \rho_m$ and the viscosity ratio $\eta = \mu_b / \mu_m$, where ρ is the fluid density, μ is
26 the viscosity and the subscripts "b" and "m" denote the "bubble" or "drop" and
27 the "matrix fluid", respectively. For a bubble in an insoluble, viscous liquid,
28 $\lambda \simeq 0$ and $\eta \simeq 0$, whereas most studies dealing with a drop in an immiscible
29 viscous liquid take $\lambda = 1$ and $\eta \simeq 1$.

30 In this work, we focus on identifying critical flow states numerically, in terms
31 of dimensionless quantities, that specify the extreme conditions at which a bub-
32 ble in shear flow first transitions from deformation to breakup. We validate our
33 numerical method by examining the sensitivity of the critical bubble deforma-
34 tion and break-up flow states with respect to the grid size. We also compare
35 with previous experimental results where the experimental data is available
36 (the high Capillary number low Reynolds' number regime). An advantage of
37 studying shear-driven bubble deformation and breakup computationally rather
38 than experimentally is that one can easily modify bubble/drop shape initial
39 conditions [39], the gravity force term[21], fluid physical properties, and the ge-
40 ometry of the (virtual) apparatus[16]. In our computations, the time-evolution
41 of the boundary between gas and liquid is tracked with a Coupled-Level-Set
42 and Volume-Of-Fluid (CLSVOF) sharp interface capturing algorithm [59, 61].
43 The rationale for the CLSVOF method is that the hybrid method represents
44 the (complex) gas-liquid interfaces with minimal volume loss (property of the
45 Volume-Of-Fluid method) and minimal error in the approximation of the sur-
46 face tension force (property of the Level-Set method). Our sharp interface
47 approach[61, 57, 27] enables us to simulate multiphase flows without artificially
48 giving the interface an empirical thickness.

49 We focus on determining critical physical conditions in which the breakup of
50 a bubble occurs in shear flow because it is important to identify the parameter
51 regimes in which a relatively simple system transitions from stable to unstable.

52 Specifically, we ascertain the critical Reynolds number (Re_c) corresponding to
53 the bubble breakup onset condition as a function of Ca .

54 In previous experimental or computational studies on the motion of bubble
55 deformation in a simple shear flow [5, 50, 36], only findings for bubble defor-
56 mation under very low Re number conditions ($Re \ll 1$) have been reported.
57 This is understandable since a low Reynolds number matrix fluid mitigates the
58 effect of gravity on distorting the comparison with the drop case. In the results
59 reported in [5], the $x - z$ cross section of the deforming bubble was close to
60 circular in their experiments. Also in the experiments in [5], the $x - z$ cross
61 section shows minimal overall bubble rise speed in the (very) viscous fluid in
62 comparison to the rate that the bubble deforms in the $y - z$ cross section. This
63 is expected since the experiments designed by [5] closely followed the following
64 basic assumptions: (i) “steady creeping flow with negligible inertial effects,” (ii)
65 “Incompressible Newtonian fluids,” (iii) “No buoyancy effects,” (iv) “No wall
66 effects.” In this work, we determine, for the first time, the critical Reynolds
67 number ($Re \gg 1$) that leads to bubble breakup. Additionally, our computa-
68 tional studies reveal characteristics that distinguish a drop’s deformation and
69 breakup processes versus those of a bubble.

70 We remark that there have been a number of computational articles on the
71 study of lift of slightly deformable bubbles[14, 31]. We reiterate, though, that
72 for bubble deformation and breakup in shear flows, only a few computational
73 articles exist: [69, 68, 53]. These previous studies mainly examined the dynamics
74 (e.g., rotation angle) of bubble deformation in shear flow. Concerning bubble
75 breakup, Wei et al. [69] presented one numerical result for a bubble breakup
76 process under the condition of Ca (capillary number) = 35. Sharifi et al[53]
77 presented two results for bubble breakup corresponding to Ca = 7.5 and Ca =
78 11.2. We point out that all of the previous computational research on bubble
79 deformation (and breakup) under shear driven flow[69, 68, 53] use the (explicit)
80 Lattice Boltzmann method. For accurately computing the tensile strength of a
81 bubble, and accurately computing threshold parameters for break-up (what we
82 do in this article, and what was not done in previous work), it is critical that a
83 numerical method directly enforces the velocity continuity condition and the gas-
84 liquid interface normal jump conditions. We contend that a projection method
85 (i.e. this paper and [73, 74, 41]) is the more appropriate (albeit slower) method
86 for our study rather than the Lattice Boltzmann method. Also, in contrast to
87 the Lattice Boltzmann method, our interface “capturing” method, the CLSVOF
88 method[59, 61], maintains the gas/liquid interface as sharp, enables accurate
89 approximation of the surface tension force, and by construction the CLSVOF
90 method preserves mass and volume within a fraction of a percent. The results
91 that we present in this article (see e.g. section 3.3.2) regarding measuring the
92 tensile strength of a bubble are unique and validated with respect to comparisons
93 with previous experimental data (where available) and grid refinement studies.
94 Each simulation on the finest resolution takes over a half a year to complete on
95 a workstation because of the following unavoidable factors: (i) the large density-
96 ratio projection method requires the solution of a large sparse, ill-conditioned,
97 matrix system at each time step, (ii) the finer the mesh, the more precise the

98 measured threshold, and right at the threshold (Taylor Deformation parameter
99 $D \approx 1$), oscillatory behaviour is observed delaying the determination of breakup
100 or not. Finally, the larger the deformation parameter D , the longer one must
101 make the computational domain (and thereby leading to larger domain aspect
102 ratio) thereby adversely effecting the condition number even more for carrying
103 our the pressure projection.

104 To highlight the mechanisms of bubble deformation and breakup in a shear
105 flow, we juxtapose the bubble results with those of a drop. We remark that
106 while the study of critical tensile strength parameters for the bubble is sparse,
107 there have been many studies for the simpler drop problem. This is because
108 the density ratio for the drop deformation case is almost one so that it is not
109 required that the continuous phase liquid be highly viscous in order to mitigate
110 buoyancy effects. For completeness, we give a brief overview of previous “tensile
111 strength” studies pertaining to drops.

112 The study of the deformation and breakup of a drop in immiscible vis-
113 cous liquids undergoing simple linear shear flow has been investigated exten-
114 sively due to its fundamental importance to emulsion processes, materials pro-
115 cessing, mixing, and reaction devices. The pioneering experimental work on
116 this problem was performed by Taylor in the early 1930s [64, 65], and the
117 subsequent theoretical and experimental progress up to the 1980s and 1990s
118 was reviewed in [43] and [56], respectively. By the 2000s, progress in com-
119 putational fluid dynamics (CFD) techniques and increased access to powerful
120 computing resources led to a surge of research focused on direct simulations
121 of this problem. In particular, detailed computational investigations of drop
122 breakup, based on a Volume-of-Fluid (VOF) method [20] were presented in
123 [33, 47, 49, 48, 28, 44, 45, 46]. Since then, the literature on computational stud-
124 ies on the deformation and breakup of a single or several drops in shear flow
125 has continued to grow [9, 23, 72, 3, 25, 10, 29, 30, 24, 19, 1, 75] and a variety
126 of numerical techniques have been developed to tackle this problem, including
127 boundary-integral approaches [8, 26], lattice Boltzmann methods [22, 29], front
128 tracking schemes [66], and interface-capturing level set methods [60].

129 Thus, a lot of studies about the deformation and breakup of a drop in sim-
130 ple linear shear have been presented so far. In contrast, few studies have been
131 conducted on bubble deformation and breakup. In the low Capillary number,
132 high Reynolds’ number regime, there are no controlled experiments or sim-
133 ulations. We reiterate why there have been few studies regarding the “tensile
134 strength” of bubbles. Experimentally, if one wants to isolate the interplay of
135 shearing force with the bubble surface tension force, in the moderate to high
136 Reynolds number regime, and low Capillary number regime, one is restricted
137 to microgravity conditions. Computational experiments are difficult too. In
138 order to accurately compute the tensile strength of a bubble, one must resort
139 to a combination of parallel computing, the multigrid preconditioned conjugate
140 gradient method[63, 61] for poorly conditioned large sparse matrix systems,
141 adaptive mesh refinement[76, 61], and a robust, volume preserving interface
142 tracking method (we use the CLSVOF method[59, 61]). These aspects of our
143 algorithm allow one to accurately simulate the balance of the restoring bubble

144 surface tension force against the driving wall shear force and at the same time,
 145 accurately simulate the evolution of the bubble shape to bubble-break-up if the
 146 given shear stress and physical properties permit it.

147 2. Problem Description

148 Figure 1(a) shows a schematic of the computational system for our studies
 149 of a bubble (or drop) in shear flow. The computational domain consists of a
 150 three-dimensional rectangular domain with the dimensions of L (length) $\times W$
 151 (width) $\times H$ (height). The size of L , W and H was determined after considera-
 152 tion of the sensitivity of numerical results to the domain size; numerical studies
 153 of domain-size dependence are presented in Section 3.3. All computational re-
 154 sults that follow were obtained from numerical solutions of the three-dimensional
 155 governing equations for gas-liquid/liquid-liquid flows. Computations are initial-
 156 ized with a spherical bubble (or drop) of radius $R = 5$ mm set at the center of
 157 the computational domain. The bubble (or drop) is then subjected to a linear
 158 shear flow generated by the motion of the top and bottom plates, which have
 159 constant velocity $+V$ and $-V$, respectively. In the interior of the domain, the
 160 initial velocity condition is assumed to be a simple linear profile and periodic
 161 boundary conditions are imposed along the x and y directions. Mathematically,
 162 the initial and boundary conditions are described as follows:

$$\phi(x, y, z, 0) = \sqrt{(x - \frac{L}{2})^2 + (y - \frac{W}{2})^2 + (z - \frac{H}{2})^2} - R \quad (1)$$

$$\mathbf{u}(x, y, z, 0) = \begin{pmatrix} \frac{2V}{H}(z - \frac{H}{2}) \\ 0 \\ 0 \end{pmatrix}$$

$$\phi(x + L, y, z, t) = \phi(x, y, z, t) \quad \phi(x, y + W, z, t) = \phi(x, y, z, t)$$

$$\mathbf{u}(x, y, H, t) = \begin{pmatrix} V \\ 0 \\ 0 \end{pmatrix} \quad \mathbf{u}(x, y, 0, t) = \begin{pmatrix} -V \\ 0 \\ 0 \end{pmatrix}$$

$$\mathbf{u}(x + L, y, z, t) = \mathbf{u}(x, y, z, t) \quad \mathbf{u}(x, y + W, z, t) = \mathbf{u}(x, y, z, t)$$

163 $\phi(x, y, z, t)$ is a material indicator function which is positive in the “matrix”
 164 fluid and negative in the bubble (or drop) fluid. $\mathbf{u}(x, y, z, t)$ is the velocity.

165 Common dimensionless physical parameters used to describe gas-liquid or
 166 liquid-liquid two-phase flows include the Reynolds (Re), Weber (We) (or Ca (=
 167 We/Re)) and Froude (Fr) numbers. Gas-Liquid and Liquid-Liquid two-phase
 168 flow problems are also determined by the density ratio λ and the viscosity ratio
 169 η . In the present study, in order to clearly isolate the effects of λ and η , and
 170 isolate the balance of the driving wall force with the bubble surface tension
 171 force, the effect of gravity is not considered ($g = 0$) so that we ignore the effect
 172 of the Fr number ($= \frac{\Gamma R}{\sqrt{g} R}$).

173 When comparing with previous drop studies, we fix $\lambda = 1$ for the drop cases.
 174 As a result, (for $\lambda = 1$) the following dimensionless physical parameters are used

175 to describe the problem of drop deformation/breakup in shear flow:

$$Re = \frac{\rho_m U R}{\mu_m}, \quad Ca = \frac{\mu_m U}{\sigma}, \quad \eta = \frac{\mu_b}{\mu_m} \quad m = \text{matrix fluid} \quad (2)$$

176 U is the velocity scale and σ denotes the surface tension. For the problem of
177 shear-induced drop deformation and breakup, the velocity is set to,

$$U = \Gamma R,$$

178 where the shear-rate is,

$$\Gamma = 2V/H.$$

179 As mentioned in the introduction, most previous drop studies set $\eta = 1$ (e.g. Li
180 et al. [33]). Thus, for comparison with previous drop deformation and breakup
181 problems, we set $\lambda = \eta = 1$ (and also neglect the effect of gravity so that
182 $g = 0$). On the other hand, in our computations for bubble deformation, we
183 set the density and viscosity of air to be $\rho_b = 1.2 \text{ kg/m}^3$ and $\mu_b = 1.8 \times 10^{-5}$
184 Pa·s respectively. We emphasize that for consistency with previous studies (Li
185 et al. [33], Rust and Manga [50], Müller-Fischer et al. [36], Komrakova et al.
186 [29], Amani et al. [1]), we computationally examine the deformation and breakup
187 of a bubble in simple linear shear flow as a function of the Re and Ca numbers.
188 That is to say, by setting $g = 0$, we are isolating the effect of only varying Re and
189 Ca on bubble deformation and breakup. In our controlled study, we determine
190 the critical Re_c versus Ca curve in which Re_c corresponds to the threshold of
191 bubble (or drop) breakup. We determine the critical Re_c versus Ca curve for
192 strategic pairs of the density ratio and viscosity ratio.

193 In our computations, the density of the matrix fluid is fixed at $\rho_m = 1000$
194 kg/m^3 . The surface tension at the bubble (drop) interface is $\sigma = 2.5 \times 10^{-2}$
195 N/m. The values of Re and Ca in our simulations are controlled by changing
196 the values of μ_m and V . Specifically, we set $\mu_m = 2.0 \times 10^{-2} \sim 6.0 \times 10^{-2}$
197 Pa·s and $V = \text{about } 1.1 \sim 1.3 \text{ m/s}$. As a consequence, for studying bubble
198 deformation and break-up, the density and viscosity ratios satisfy $\lambda = 1.2 \times 10^{-3}$
199 and $\eta < 1.0 \times 10^{-3}$.

200 Remark: if we were to apply “Earth” gravity conditions in our simulations,
201 then $g = 9.8 \text{ m/s}^2$, and the Froude number (Fr) is in the range $Fr = 1.7 \sim 1.9$.
202 Although these values of Fr are not so large, the effect of gravity (inducing
203 bubble rise motion) may not be completely negligible. However, bubbles in
204 our computations reach the breakup by way of deformation very quickly at t
205 = about 0.5 s. Accordingly, it is expected that the effect of gravity (inducing
206 bubble rise motion) can be small for the behavior of bubble deformation and
207 breakup around the critical Re number conditions determined in our study.

208 3. Numerical Analysis

209 3.1. Numerical method and governing equations

210 Numerical results were obtained using the interface capturing Coupled Level
211 Set and Volume of Fluid (CLSVOF) method (Sussman and Puckett [59], Suss-

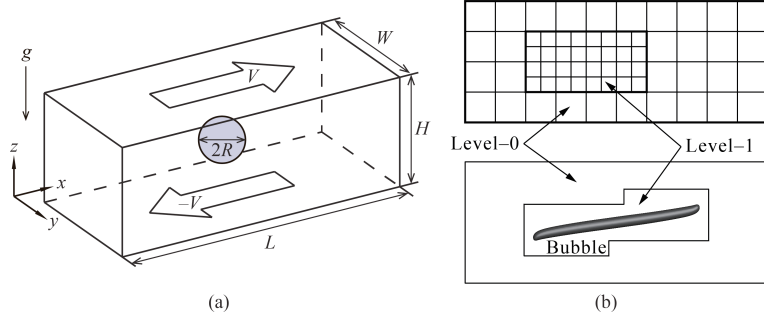


Figure 1: (a) Computational domain schematic for a bubble or drop in shear flow. Gravity is set to zero in our computations in order to isolate the effects of density and viscosity ratios. (b) (upper panel) a two-level adaptive mesh refinement (AMR) grid schematic corresponding to one of our simulations; (lower panel) snapshot of bubble deformation in simple linear shear flow.

man et al. [61]), which is based on a fixed grid finite volume algorithm. The CLSVOF method is a robust numerical technique that combines some of the advantages of the Volume of Fluid (VOF) method (Hirt and Nichols [20]) and the Level Set (LS) (Sussman et al. [60]) method while overcoming their weaknesses. In the VOF method, the Volume Fraction function, F , is used to represent the interface. The values of F correspond to the volume fraction of liquid in a given computational cell. In other words, $F = 0$ when a computational cell contains only gas and $F = 1$ when a computational cell contains only liquid. If $0 < F < 1$, then a computational cell contains the gas-liquid interface. The VOF method has an advantage over the LS method in that accurate algorithms for advecting F can be applied so that mass/volume is conserved up to machine precision while still maintaining a sharp representation of the interface. On the other hand, the disadvantage of the VOF method in comparison to the LS method is that tangled and difficult reconstruction procedures are required for determining the slope of the piecewise linear VOF reconstructed interface. In the LS method, the signed distance function ϕ (LS function) is used to track the interface. The interface is implicitly represented by the set of points in which $\phi = 0$. Liquid and gas regions are defined as $\phi > 0$ in the liquid and $\phi < 0$ in the gas, respectively. One of the advantages of the LS method is that one can track and represent smoothly the interface, but the LS method has the disadvantage that mass/volume is not explicitly conserved. In the CLSVOF method, the coupling between the LS function and the VOF function occurs when computing the normal of the reconstructed interface in the VOF calculation process and also when assigning the LS function with the exact signed normal distance to the reconstructed interface in the LS calculation process. That is to say, the piecewise linear approximation (the volume-of-fluid reconstruction step) for the VOF method is determined using the unit normal vector (\mathbf{n}) estimated from information of the LS function. By taking advantage of both methods, the evolution of the liquid-gas interface location can be computationally captured in

such a way so that volume/mass is preserved to machine precision and at the same time, the interface normals and the surface tension force (which is proportional to the interface curvature) can be straightforwardly derived from the smooth level set function.

In our studies, the two-phase fluid flow is comprised of air and a viscous Newtonian liquid. The Heaviside function, $\mathcal{H}(\phi)$, which is defined as

$$\mathcal{H}(\phi) = \begin{cases} 1 & \phi \geq 0 \\ 0 & \phi < 0 \end{cases} \quad (3)$$

will be used below to distinguish each of the two fluids. A single set of three-dimensional equations governs the motion of both fluids, which are taken to be incompressible, and consists of the continuity equation and the Navier-Stokes equations with surface tension forces:

$$\nabla \cdot \mathbf{u} = 0 \quad (4)$$

$$\frac{\partial \mathbf{u}}{\partial t} + (\mathbf{u} \cdot \nabla) \mathbf{u} = \frac{1}{\rho} \nabla \cdot (-p \mathbf{I} + 2\mu \mathbf{D}) + \mathbf{g} - \frac{\sigma \kappa}{\rho} \nabla \mathcal{H} \quad (5)$$

We note that our method is a “sharp interface method[61, 57, 27]. Thereby we do not need to specify an empirical interface thickness parameter[60, 59].

\mathbf{u} is the velocity vector, t represents time, p is the pressure, \mathbf{I} is the unit tensor, \mathbf{D} is the rate of deformation tensor ($\mathbf{D} = \frac{1}{2}(\nabla \mathbf{u} + (\nabla \mathbf{u})^T)$), ρ is the density, μ is the viscosity, κ is the interfacial curvature, and the Heaviside function $\mathcal{H}(\phi)$ is a function of the level set (LS) function ϕ . The singular Heaviside gradient term in the right-hand side of equation (5) is a body force representing the surface tension force and is equivalent to specifying that the jump in the normal stress is equal to $\sigma \kappa$ (Tanguy et al. [62]). The surface tension force expressed by the singular Heaviside gradient term acts only on the gas-liquid interface. The sharp interface “Ghost Fluid Method” (Kang et al. [27]) is used to discretize the gradient of the Heaviside function as it appears in the surface tension force term. This force, upon discretization, is only non-zero across cells in which the level set function changes sign.

The interfacial curvature κ is computed with second-order accuracy directly from the volume-of-fluid (VOF) function and the level set function using the height function technique (Sussman [57], Sussman et al. [61]). We note that we would get the same results if we compute κ directly from the LS function using the “level set” height function technique.

Since ρ and μ are taken to be constant in each fluid, with a jump at the interface, they can be expressed in terms of the Heaviside function,

$$\rho = \rho_m \mathcal{H} + \rho_b (1 - \mathcal{H}), \quad \mu = \mu_m \mathcal{H} + \mu_b (1 - \mathcal{H}). \quad (6)$$

The subscripts “b” and “m” refer to “bubble” (or drop) and “matrix fluid.” To represent the free surface with the CLSVOF method, we must evolve the solution to both the VOF equation for F and the LS equation for ϕ :

$$\frac{\partial F}{\partial t} + (\mathbf{u} \cdot \nabla) F = 0, \quad \frac{\partial \phi}{\partial t} + (\mathbf{u} \cdot \nabla) \phi = 0. \quad (7)$$

268 In all computations, the discretized variables p , ϕ , and F are located at the
 269 cell centers, and the discrete velocity variable \mathbf{u} is located at the cell face cen-
 270 ters. Our computations are performed using an overall second-order accurate
 271 hydrodynamic scheme. The spatial discretization uses second-order accurate,
 272 slope-limited, upwind techniques for the nonlinear advective terms. The ve-
 273 locity and pressure fields are computed using an implicit pressure projection
 274 procedure.

275 The temporal discretization of our numerical method is an operator split
 276 projection method as described by Sussman et al. [61]. An outline of our method
 277 is as follows (see Sussman et al. [61], section 4, for more details):

All Steps. Timestep

278 The timestep, Δt , is governed by the CFL condition and surface tension
 279 (section 5.7 of Sussman et al. [61]):

$$\Delta t < \min_{i,j,k} \left(\frac{\Delta x}{2|U^n|}, \frac{1}{2} \sqrt{\frac{\rho^L}{8\pi\sigma}} \Delta x^{3/2} \right)$$

Step 1. CLSVOF interface advection

$$\begin{aligned}\phi^{n+1} &= \phi^n - \Delta t [\mathbf{u} \cdot \nabla \phi]^n \\ F^{n+1} &= F^n - \Delta t [\mathbf{u} \cdot \nabla F]^n\end{aligned}$$

Step 2. Nonlinear advective force terms

$$\mathcal{A} = [\mathbf{u} \cdot \nabla \mathbf{u}]^n$$

Step 3. Viscosity force

$$\frac{\mathbf{u}^* - \mathbf{u}^n}{\Delta t} = -\mathcal{A} + g\vec{z} - [\nabla p/\rho]^n + \frac{1}{2} \frac{\nabla \cdot (2\mu \mathbf{D}^n) + \nabla \cdot (2\mu \mathbf{D}^*)}{\rho}$$

280 Step 4. Pressure projection and ghost fluid surface tension algorithm

$$\mathbf{V} = \mathbf{u}^n + \Delta t (-\mathcal{A} + g\vec{z} + \frac{1}{2} \frac{\nabla \cdot (2\mu \mathbf{D}^n) + \nabla \cdot (2\mu \mathbf{D}^*)}{\rho})$$

281

$$\mathbf{V} = \mathbf{V} - \Delta t \frac{\sigma \kappa(\phi^{n+1})}{\rho} \nabla \mathcal{H}(\phi^{n+1})$$

282

$$\nabla \cdot \frac{\nabla p}{\rho} = \frac{1}{\Delta t} \nabla \cdot \mathbf{V}$$

283

$$\mathbf{u}^{n+1} = \mathbf{V} - \Delta t \frac{\nabla p}{\rho}$$

To make efficient use of computational resources, our numerical simulations utilize an adaptive hierarchy of grids based on a dynamic adaptive mesh refinement (AMR) technique (Sussman et al. [58]). Adaptive grids are dynamically adjusted based on the location of the deforming gas-liquid interface. In the AMR technique, the grid resolution is increased in regions near the interface, while a coarser grid is used where the flow is relatively steady. The upper panel of Figure 1(b) displays a schematic view of the hierarchical grid structure, and the lower panel corresponds to an actual computational example corresponding to bubble deformation in simple linear shear flow. In general, the mesh hierarchy is composed of different levels of refinement ranging from coarsest $\ell = 0$ (“level-0”) to finest $\ell = \ell_{\max}$ (“level- ℓ_{\max} ”). The refinement ratio of one grid size ($\Delta x = \Delta y = \Delta z$) to the next finer level is two so that $\Delta x^{\ell+1} = 0.5\Delta x^\ell$. All computations in this study used an AMR system with a maximum prescribed level $\ell_{\max} = 1$ (as illustrated in the upper panel of Figure 1(b)). In our adaptive mesh refinement algorithm, the velocity in the coarse grid cells that neighbor fine grid cells are interpolated from the coarse grid using bilinear interpolation to initialize “ghost” fine cells. Thus, the bilinear interpolation procedure produces interpolated fine-grid data as a linear combination of the coarse-grid data.

Remark 1: Due to time step stability constraints, the variable density pressure projection process, and computed bubble shapes with high aspect ratio, we find that our simulations can take over six months. We have experimented with (a) decreasing the “error buffer” parameter from two cells to one (radius of cells to be tagged when a given cell is tagged for adaptivity) and (b) relaxing the condition that the bubble-liquid interface be wholly contained on the finest adaptive level. Unfortunately, we have found that these steps lead to poorer accuracy. This “diminishing returns” phenomenon is expected for low Mach number flows in which the incompressible flow equations are characterized by non-local behavior. We refer the reader to the following research[34] in which it has been found through a systematic study that using an AMR grid can be less accurate than a case with a uniform fine grid (luckily, that is not the case here). To summarize, we have found that each further refinement of the grid will multiply the simulation time by about eight (a factor of 4 due to spatial refinement and a factor of 2 due to temporal refinement).

Remark 2: We believe that including a customized sub-scale model right at the point of bubble break-up is unnecessary because the driving shear force is uniformly applied in the time variable instead of impulsively applied. We are aware of research for predicting whether droplets merge or bounce[32] that necessitate the inclusion of a sub-scale model, but that research is not applicable in our case. Previous studies on the shear flow-driven breakup of bubbles or drops have not incorporated customized subscale models[33, 29, 1].

3.2. Validation of the numerical method

The effectiveness of our sharp interface computational method has been demonstrated via grid refinement studies and comparison with experiments for the complicated rising motion of single bubbles and drops in viscous liquids Ohta and Sussman [41], Ohta et al. [37, 38, 42], Stewart et al. [55], Sussman

et al. [61], the simulation of atomization in a realistic diesel injector[2], and the simulation of bubble formation due to the injection of gas through a nozzle[40]. In this section, the accuracy of our computational method will be verified for the problem of shear-induced deformation of a drop and bubble.

First, we compare quantitatively against the steady-state drop deformation results reported by Li et al. [33]. The shape of a deformed drop in simple linear shear flow is described in terms of the Taylor deformation parameter $D=(a-b)/(a+b)$, where a and b are the major and minor axes of the deformed drop, respectively. For consistency, we perform numerical simulations using CLSVOF over the same computational domain and grid size used in Li et al. [33], which has dimensions $L(8R) \times W(4R) \times H(8R)$ (recall that R is the bubble/drop radius) and a level-0 grid size $\Delta x = \Delta y = \Delta z = R/8$; our two-level AMR grid structure also uses a finer level-1 grid size $\Delta x^{\ell=1} = \Delta y^{\ell=1} = \Delta z^{\ell=1} = R/16$. Numerical results are listed in Table 1 for D as a function of Re , with $Ca = 0.3$ and $\lambda = \eta = 1$ fixed in every case. The results in Table 1 compare computations using our CLSVOF algorithm with corresponding results obtained with the VOF method used in Li et al. [33].

Table 1: Comparison of the Taylor deformation parameter D for a drop as a function of Re ($Ca = 0.3$, $\lambda = \eta = 1$). In all cases, the domain size is $L(8R) \times W(4R) \times H(8R)$, where R is the drop radius. The CLSVOF method computations used a two-level AMR computational domain with a level-0 discretization $\Delta x^{\ell=0} = \Delta y^{\ell=0} = \Delta z^{\ell=0} = R/8$ and a level-1 discretization $\Delta x^{\ell=1} = \Delta y^{\ell=1} = \Delta z^{\ell=1} = R/16$.

Reynolds number	0.1	0.5	0.6	0.75
D (Li et al. [33])	0.3968	0.45	0.4768	Breakup
D (Our study)	0.3960	0.4570	0.4758	Breakup

Next, we report the results of validation tests conducted with our computational method; we compare our results with the “bubble deformation in simple linear shear flow” results reported by Müller-Fischer et al. [36]. Müller-Fischer et al. [36] experimentally inquired into the bubble deformation under the condition of $Re \approx 0$. In our study, we computed the bubble deformation on a computational domain with dimensions $L(12R) \times W(6R) \times H(6R)$ and a computational grid in which the finest level grid size was $\Delta x^{\ell=1} = \Delta y^{\ell=1} = \Delta z^{\ell=1} = R/16$. Computations were performed for the conditions of $Ca = 0.96$ and $Ca = 1.63$ with $Re \approx 0$ ($Re = 5.0 \times 10^{-4}$), $\lambda = 1.2 \times 10^{-3}$ and $\eta \leq 1.2 \times 10^{-6}$. The prescribed parameters are consistent with the experimental conditions by Müller-Fischer et al. [36]. Comparisons of our numerical results and previous experimental results (Müller-Fischer et al. [36]) are tabulated in Table 2. Additionally, in Table 2, we list experimental results with the condition of $Re \approx 0$ and $\lambda \approx \eta \approx 0$ by Rust and Manga [50]. These experimental values were obtained from the graph showing the relation of D vs Re (Rust and Manga [50]). As is clear from Table 2, our numerical results predicted larger values of D than experimental ones reported by Müller-Fischer et al. [36]. Nevertheless, our numerical results are very close to the experimental results by Rust and Manga [50], which

364 emphasizes the intrinsic difficulties associated with experimental investigations
 365 of bubble dynamics, even in simple linear shear flow. These comparisons suggest
 366 that our computational method is effective and robust at reproducing bubble
 dynamics in simple linear shear flow.

Table 2: Comparison of D for a bubble as a function of Ca ($Re \approx 0$, $\lambda \approx \eta \approx 0$). In all cases, the domain size is $L(12R) \times W(6R) \times H(6R)$. The CLSVOF computations used a two-level AMR computational domain with a level-0 discretization $\Delta x^{\ell=0} = \Delta y^{\ell=0} = \Delta z^{\ell=0} = R/8$ and a level-1 discretization $\Delta x^{\ell=1} = \Delta y^{\ell=1} = \Delta z^{\ell=1} = R/16$.

Capillary number	0.96	1.63
D (Müller-Fischer et al. [36])	0.37	0.58
D (Rust and Manga [50])	0.71 ± 0.05	0.81 ± 0.02
D (Our study $\Delta x^{\ell=1} = R/16$)	0.63	0.71

367

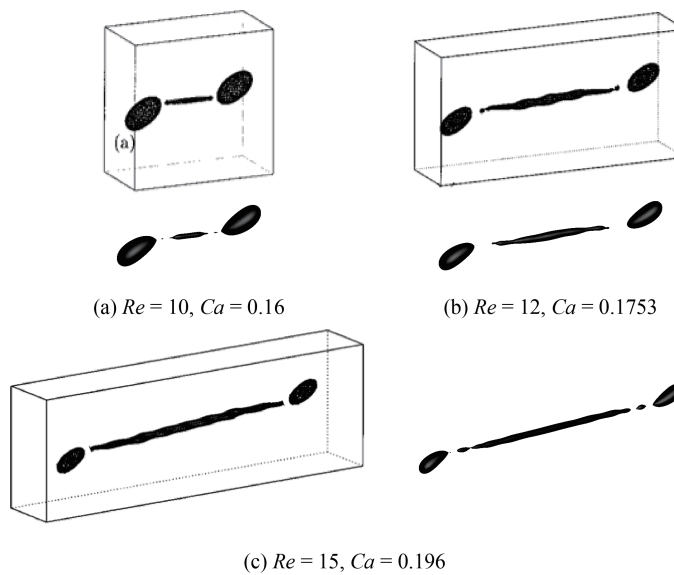


Figure 2: Comparison with results reported in Renardy and Cristini [49] (shown in bounding boxes) for drop breakup in shear flow. In Renardy and Cristini [49], the computational domain dimensions were $W = 4R$, $H = 8R$, and L was varied depending on the Re and Ca conditions. The grid size in Renardy and Cristini [49] was set to $\Delta x = \Delta y = \Delta z = R/8$. Reprinted with permission from reference Renardy and Cristini [49]. Copyright 2001, AIP Publishing. The results obtained with our CLSVOF algorithm, corresponding to each case in reference Renardy and Cristini [49], are shown without the bounding boxes. The CLSVOF method used a two-level AMR computational domain with a level-0 discretization $\Delta x^{\ell=0} = \Delta y^{\ell=0} = \Delta z^{\ell=0} = R/8$ and a level-1 discretization $\Delta x^{\ell=1} = \Delta y^{\ell=1} = \Delta z^{\ell=1} = R/16$. The onset of drop breakup is demonstrated for (a) $Re = 10$, $Ca = 0.16$, (b) $Re = 12$, $Ca = 0.1753$, and (c) $Re = 15$, $Ca = 0.196$. For all three Re and Ca conditions, $\lambda = \eta = 1$.

368

Finally, we compare numerical results from our method with the numerical

results for drop breakup reported in Renardy and Cristini [49]. Figure 2 demonstrates drop breakup with pinch-off behavior for three Re and Ca conditions and with constant values of $\lambda = \eta = 1$ for all cases. The three cases that we consider correspond to (a) $Re = 10, Ca = 0.16$, (b) $Re = 12, Ca = 0.1753$, and (c) $Re = 15, Ca = 0.196$, and which are illustrated in Figures 2(a)-(c), respectively. The results reported in Renardy and Cristini [49], which were obtained with a VOF method, are shown inside boxes while results obtained with our CLSVOF approach are displayed outside boxes. In the computations presented in Renardy and Cristini [49], the dimensions $W = 4R$ and $H = 8R$ were fixed, while L was changed depending on Re and Ca conditions, and the grid size was set to $\Delta x = \Delta y = \Delta z = R/8$. To compare with their results, we performed simulations with the CLSVOF method over a two-level AMR computational domain of the same dimensions and the same level-0 discretization: $\Delta x^{\ell=0} = \Delta y^{\ell=0} = \Delta z^{\ell=0} = R/8$; we set the finer level-1 grid size $\Delta x^{\ell=1} = \Delta y^{\ell=1} = \Delta z^{\ell=1} = R/16$. The results shown in Figure 2 verify that our numerical approach can reproduce the same drop breakup behavior presented in Renardy and Cristini [49]. Slight differences between the results can be attributed to the increased resolution used in our study in the level-1 grid around the elongated drop.

The numerical validation studies performed in this section and the following section demonstrate that our numerical method can reliably determine the transition regions at which shear-induced bubble or drop deformation leads to breakup. In the next section, we demonstrate that we can expect an error of 3% for predicting the transition to break-up. The analysis in this section and the following also indicate that the error is reduced by a factor of 2 each time the grid is refined by a factor of 2. We reiterate that we have found at least a factor of 2 error reduction for each grid refinement in many multiphase flow problems involving complex interface deformation and breakup; see Ohta and Sussman [41], Ohta et al. [37, 38, 42], Stewart et al. [55], Sussman et al. [61], Arienti et al. [2], Ohta et al. [40].

3.3. Consideration of domain and grid sizes

3.3.1. Selecting the appropriate domain size

The computational domain size used in numerical studies can affect the behavior of drop deformation and breakup. Referring to Figure 1(a), with an appropriately large domain length L and a fixed width $W = 4R$, the effect of the height H on drop behavior was examined in Li et al. [33] for Stokes flows and various Ca conditions and in Komrakova et al. [29] for $Re = 1$ and $Ca = 0.27$. Other related studies investigated drop breakup sensitivity (Renardy and Cristini [47]) and drop deformation sensitivity (Renardy et al. [48]) with respect to the entire domain size. Here, we investigate the drop dynamics sensitivity to domain size around the critical Reynolds number $Re_c = 0.75$. Specifically, we consider domain size sensitivity for the condition of $Re = 0.75, Ca = 0.3$, and $\lambda = \eta = 1$, a condition used in the comparison studies of the previous section. As shown in Table 1, the drop breaks up for the condition of $Re = 0.75$

Table 3: Comparison of the Taylor deformation parameter D for a drop as a function of domain size ($Re = 0.75$, $Ca = 0.3$, $\lambda = \eta = 1$). CLSVOF method computations used a two-level AMR computational domain with a level-0 discretization $\Delta x^{\ell=0} = \Delta y^{\ell=0} = \Delta z^{\ell=0} = R/8$ and a level-1 discretization $\Delta x^{\ell=1} = \Delta y^{\ell=1} = \Delta z^{\ell=1} = R/16$.

System	Domain size ($L \times W \times H$)	D
System 1	$8R \times 4R \times 8R$	Breakup
System 2	$12R \times 4R \times 8R$	Breakup
System 3	$8R \times 4R \times 6R$	0.541
System 4	$8R \times 6R \times 6R$	0.466
System 5	$8R \times 8R \times 8R$	0.460
System 6	$8R \times 16R \times 16R$	0.460

and $Ca = 0.3$ with a domain size of $L(8R) \times W(4R) \times H(8R)$. Results for domain size sensitivity for six domain systems, all of which use a level-1 grid size $\Delta x^{\ell=1} = \Delta y^{\ell=1} = \Delta z^{\ell=1} = R/16$, are tabulated in Table 3. Note that the domain size used in the comparison study (Table 1) corresponds to System 1.

The results in Table 3 suggest that drop deformation is promoted when we use a domain size with $W = 4R$. In contrast, the drop does not break up and becomes stable with a deformed shape if we set L large enough and $W \geq 6R$ and $H \geq 6R$. Since the value of D for the domain size $L(8R) \times W(6R) \times H(6R)$ differs by only 1.3% with the value for the domain size of $L(8R) \times W(16R) \times H(16R)$, in the results that follow we set the width to $W = 6R$ and the height to $H = 6R$ to minimize the number of computational grid nodes along those directions. To determine the critical Reynolds number Re_c (with $Ca = 0.3$), we consider a domain size of $L(24R) \times W(6R) \times H(6R)$, and we find that the drop reaches a stable state with deformation parameter $D=0.549$ for $Re = 1.0$, while a value of $Re = 1.1$ leads to drop breakup.

3.3.2. Selecting the appropriate grid size

The grid size and adaptive meshing strategy we adopt are chosen to answer the research question as to the conditions that determine whether a bubble in shear flow will break up. In such a case, we must accurately capture the balance of forces between the (non-local) force exerted from the wall-driven flow acting against the interfacial surface tension force. The accuracy of the “Critical Reynolds Number” depends on the largest Taylor Deformation parameter D that is supported by the grid (see e.g., Figures 8 and 11). As we report here, we have found that as long as the grid size is fine enough to support a Taylor Deformation parameter $D < 0.95$, then the transition region (i.e. “Critical Reynolds number”) (see Figures 3 and 12) will be captured with a tolerance of three percent. The simulation time would become impractical if we were to try further to improve the accuracy of the “critical Reynolds number”. A smaller tolerance would necessitate a larger supported Deformation parameter D , which would in turn, necessitate a higher aspect ratio computational domain, increased droplet surface area at break-up, increased number of time steps, and

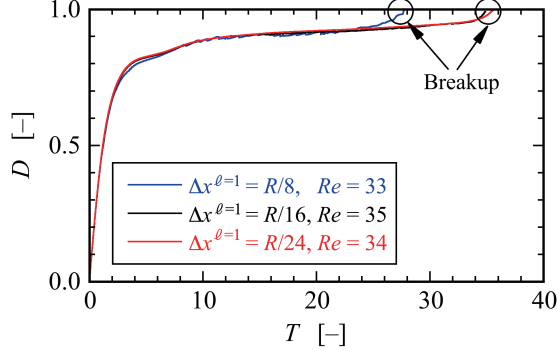


Figure 3: Time evolution of the deformation parameter D versus dimensionless time $T = \Gamma t$ for a bubble, obtained with three grid systems at different resolutions. All three resolutions use a two-level AMR grid with an effective fine resolution grid size $\Delta x^{\ell=1} = \Delta y^{\ell=1} = \Delta z^{\ell=1}$. The evolution of D using the first system, where $\Delta x^{\ell=1} = R/8$, is shown in blue and it predicts that bubble breakup occurs at a Reynolds number $Re = 33$. The evolution of D using the second system, where $\Delta x^{\ell=1} = R/16$, is shown in black and it predicts that bubble breakup occurs at a Reynolds number $Re = 35$. Results with the third system, shown in red, use $\Delta x^{\ell=1} = R/24$, and they predict that breakup occurs at $Re = 34$. The capillary number corresponding to these results is $Ca = 1.0$. ($\lambda = 1.2 \times 10^{-3}$, $\eta < 1.0 \times 10^{-3}$)

444 higher resolution for representing the drop/bubble at its thinnest point.

445 We distinguish between our present research and the research found in the
446 work of Zhang et al. [73, 74] on predicting the conditions for bubble mergers.
447 Even in the most extreme cases for mergers, the largest Deformation
448 parameter never exceeds 0.4 in Zhang et al. [73]. In summary, our gridding re-
449 quires necessitate grid points distributed relatively evenly throughout the
450 computational domain when a bubble is stretched to a $D = 0.9$ Deformation,
451 whereas in Zhang et al. [73], the gridding strategy necessitates a more localized
452 approach.

453 The numerical results presented in this and the previous section used a
454 finest-level grid size set to $\Delta x^{\ell=1} (= \Delta y^{\ell=1} = \Delta z^{\ell=1}) = R/16$. To verify the
455 adequacy of this grid resolution, we present grid refinement results for a bubble
456 breakup simulation with $Ca = 1.0$, which corresponds to the most deformable
457 and stretchable bubble case considered in our numerical studies. We use three
458 different grid systems, (i) $\Delta x^{\ell=1} = R/8$, (ii) $\Delta x^{\ell=1} = R/16$, and (iii) $\Delta x^{\ell=1} =$
459 $R/24$, in order to determine Re_c . Figure 3 shows the time evolution of the
460 deformation parameter D over time for the three grid systems; the x -axis is a
461 dimensionless time defined by $T = \Gamma t$ and the y -axis is D . The results show that
462 bubble breakup occurs at $Re_c = 35$ for the grid system with $\Delta x^{\ell=1} = R/16$,
463 while the finer computational grid with $\Delta x^{\ell=1} = R/24$ predicts a critical value of
464 $Re_c = 34$. For the $\Delta x^{\ell=1} = R/8$ results, it is clear that the $R/8$ resolution is too
465 coarse to capture the proper break-up time, albeit the critical Reynolds' number,
466 $Re_c = 33$, was still close to the finer grid resolution cases. Note that although
467 the time evolution of D for the two finer resolution systems ($R/16$ and $R/24$)

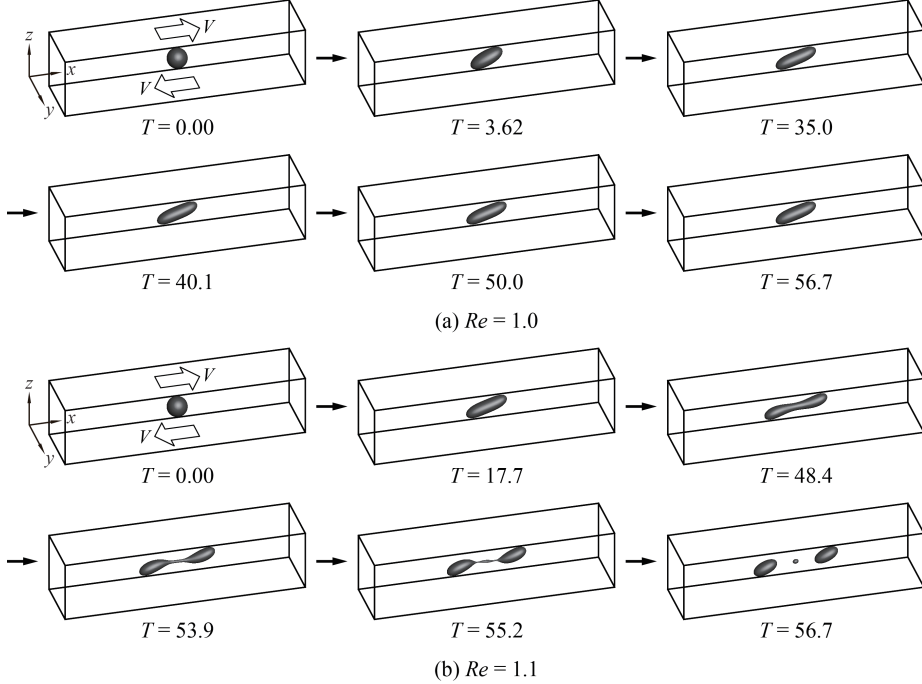


Figure 4: Time evolution of drop deformation and breakup in shear flow at the condition of $Ca = 0.3$ with (a) $Re = 1.0$ and (b) $Re = 1.1$. The “drop” critical Reynolds number corresponding to $Ca = 0.3$ is $1.0 < Re_c < 1.1$. ($\lambda = \eta = 1.0$)

is consistent between the two (the predicted critical Reynolds numbers differ by $\sim 3\%$), the computational time using the grid system with $\Delta x^{\ell=1} = R/24$ was more than 6 times longer than the one based on the coarser system with $\Delta x^{\ell=1} = R/16$. We remark that in our search for Re_c , we considered a wide range of values of Ca , and we found it necessary to use a large L ($\sim 24R$) since for certain shear flows the bubble can stretch significantly without breaking up. Nevertheless, for the conditions presented in this section, the results indicate that our numerical approach, even with a finest-level resolution set to $\Delta x^{\ell=1} = R/16$, is capable of accurately reproducing bubble deformation and breakup without sacrificing any essential dynamical features.

4. Results and Discussion

4.1. Drop deformation and breakup

To illustrate the differences in deformation and breakup between a drop and a bubble around critical conditions, we first present numerical results for drop deformation. The time evolution of drop deformation and breakup in simple linear shear flow for two conditions is shown in Figure 4.1; the first case, shown in Figure 4.1(a), uses $Ca = 0.3$ and $Re = 1.0$, while the second case,

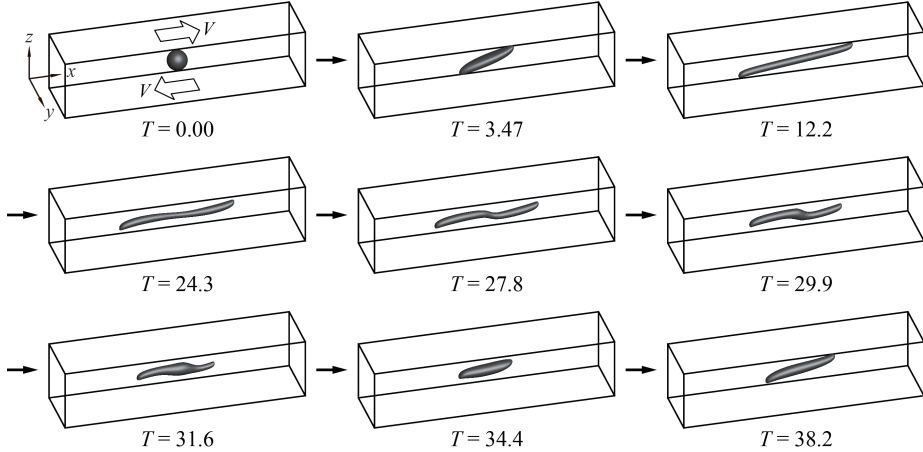


Figure 5: Time evolution of bubble deformation in shear flow at the condition of $Ca = 0.3$ and $Re = 92$. The “bubble” critical Reynolds number corresponding to $Ca = 0.3$ is $92 < Re_c < 93$. In contrast to the drop deformation case, when Re is slightly below Re_c (See Figure 4.1 $Re = 1.0$ for the drop case), the bubble shape will not reach a steady shape, instead the bubble shape alternates between the shapes “slightly stretched” ($T = 3.47$), fully stretched and “doglegged” ($T = 27.8$) and “almost” back to the original “slightly stretched” case ($T = 34.4$). ($\lambda = 1.2 \times 10^{-3}$, $\eta < 1.0 \times 10^{-3}$)

485 depicted in Figure 4.1(b), uses $Ca = 0.3$ and $Re = 1.1$. Using a domain size
 486 of $L(24R) \times W(6R) \times H(6R)$, in the case with $Re = 1.0$, the drop gradually
 487 deforms and finally attains a stable deformed state.

488 After $T = 35.0$, the drop remains a stable deformed state with $D = 0.549$.
 489 Over the same domain, for the case with $Re = 1.1$, the “mother” drop elongates
 490 over time, and the volume at the ends of the deforming drop expands; both ends
 491 become bulb-shaped. As time progresses, particularly over the time interval
 492 $48.4 \leq T \leq 55.2$, a thread-bridge forms between the bulbous ends, and the
 493 thread-bridge becomes thinner. Finally, at around the dimensionless time $T \sim$
 494 56.7, the mother drop breaks up, forming two “daughter” drops through the
 495 pinch-off; one satellite drop is also generated between the pinched-off daughter
 496 drops.

497 4.2. Bubble deformation and breakup

498 Next, we present numerical results that illustrate the conditions that lead to
 499 bubble deformation without breakup and conditions where the bubble deforms
 500 and ultimately breaks up. The time evolution of shear-induced bubble defor-
 501 mation without breakup at the condition of $Ca = 0.3$ and $Re = 92$ is depicted
 502 in Figure 5 and the bubble breakup process with flow condition of $Ca = 0.3$
 503 and $Re = 93$ is illustrated in Figure 6. The results indicate that the critical
 504 Reynolds number is approximately $Re_c = 93$ (with $Ca = 0.3$). A comparison
 505 with the drop breakup dynamics presented in Section 4.1 and the correspond-
 506 ing processes for bubble deformation and breakup exhibit very distinct features.

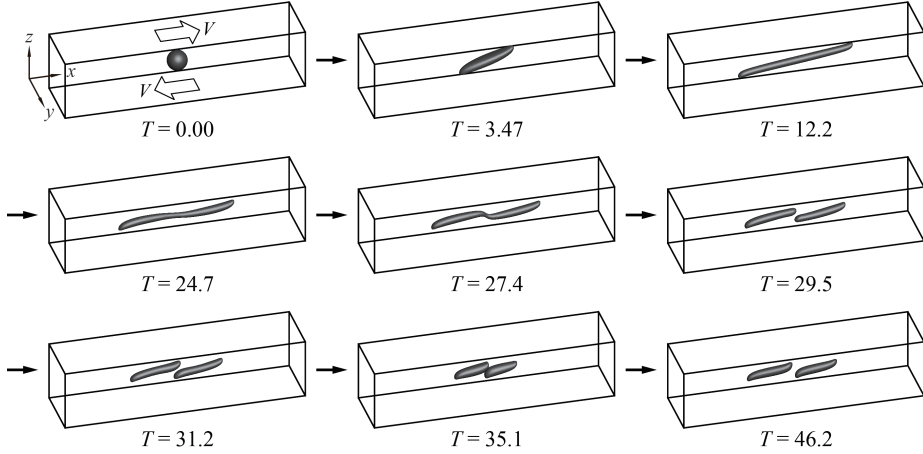


Figure 6: Time evolution of bubble deformation in shear flow at the condition of $Ca = 0.3$ and $Re = 93$. The “bubble” critical Reynolds number corresponding to $Ca = 0.3$ is $92 < Re_c < 93$. ($\lambda = 1.2 \times 10^{-3}$, $\eta < 1.0 \times 10^{-3}$)

507 First, we note that a relatively large shear force magnitude is required for bubble
 508 breakup ($\lambda = 1.2 \times 10^{-3}$, $\eta < 1.0 \times 10^{-3}$) compared with the case of the drop (λ
 509 $= \eta = 1$). Then, for the same value of $Ca = 0.3$, the critical Reynolds number
 510 for the bubble is around 85 times larger than that for the drop. Focusing on the
 511 bubble dynamics with no-breakup (Figure 5), the results show that the bub-
 512 ble is noticeably elongated in the x -direction at the early stages ($T \leq 24.3$) of
 513 bubble deformation, but the bubble does not develop the bulb-like shape (large
 514 volume areas) at both ends as observed in the drop deformation process. It is
 515 also evident that the ends of the deforming bubble develop cusped shapes under
 516 the influence of the strong shear flow.

517 In providing a more detailed description, very large shear forces are required
 518 to deform the bubble because $\lambda \simeq 0$ and $\eta \simeq 0$. Thus, the bubble undergoing
 519 large shear forces at $T > 0$ is largely stretched along the shear flow direction,
 520 and the very long elongated bubble with cusped shapes is formed. Accordingly,
 521 the bubble finally breaks up through the elongated shape without forming a
 522 bulb-like shape. A noteworthy feature of the non-breaking bubble is that it
 523 does not settle into a deformed stable state as in the case of drop deformation
 524 presented in Figure 4.1(a). After an initial elongation process, the bubble enters
 525 a shrinking phase ($T = 27.8$) where the doglegged shape formed at the center
 526 of the bubble returns to a smaller deformed shape ($T = 34.4$) that is similar to
 527 its earlier shape ($T = 3.47$). However, when we compare the early deformed
 528 bubble shape at $T = 3.47$ with the shape at $T = 34.4$, it is clear that the shapes
 529 are not identical. Following the shrinking phase, the bubble stretches again
 530 ($T = 38.2$) and oscillates between its elongated shape and shortened geometry.

531 For the case of bubble breakup (Figure 6), we observe that the deformation

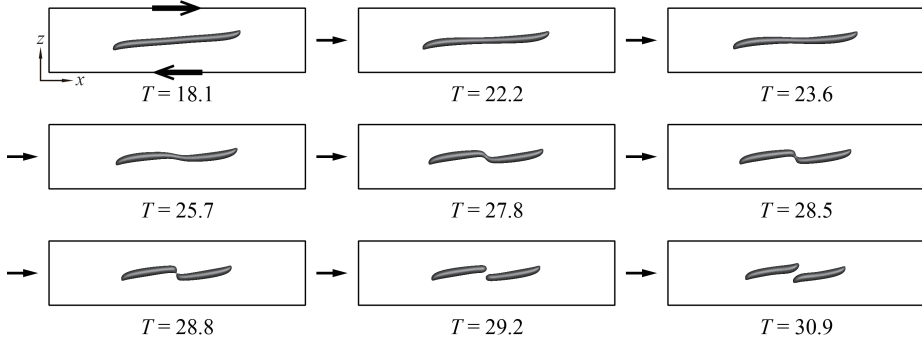


Figure 7: Detail of bubble breakup process in shear flow at the condition of $Ca = 0.3$ and $Re = 93$. The “bubble” critical Reynolds number corresponding to $Ca = 0.3$ is $92 < Re_c < 93$. ($\lambda = 1.2 \times 10^{-3}$, $\eta < 1.0 \times 10^{-3}$)

process is almost the same as the no-breakup case until the doglegged shape is formed at $T \sim 27.4$. The bubble finally breaks during the time interval $27.7 \leq T \leq 29.5$. For a closer examination of the bubble breakup process, a detailed panel of cross-sectional slices in the xz -plane through the bubble shape center is presented in Figure 7. The images displayed in Figure 7, which are taken at shorter time intervals than those shown in Fig. 6, reveal that the bubble breaks up into two daughter bubbles due to the pinch off at the thread-bridge part of the doglegged shape during the shrinking process ($T = 28.5 \sim 28.8$). After breaking up, the two daughter bubbles migrate to the center: the left daughter bubble moves toward the right side of the domain and the right daughter bubble moves to the left side (see results for $T = 29.5 \sim 35.1$ in Figure 6 and for $T = 28.8 \sim 30.9$ in Figure 7). The two daughter bubbles then momentarily congregate near the domain center ($T = 35.1$ in Figure 6), before they slowly start to separate: the left daughter bubble moves to the left, and the right daughter bubble moves to the right ($T = 46.2$ in Figure 6). The results demonstrate that the bubble breakup process is markedly different from the analogous drop breakup process with $\lambda = 1$ and $\eta = 1$. Note that the appearance of deformation and breakup of the drop will largely depend on the viscosity ratios.

4.3. Shear stress acting on the bubble

The previous section discussed bubble deformation and breakup. Large deformation and breakup of the bubble are expected to be closely related to the state of shear stress acting on the bubble. Figure 8 shows the shear stress profile around a bubble for two Reynolds numbers under the condition of $Ca = 0.3$: Reynolds number equal to 50 and 93. The shear stress profile on the left corresponds to the case of $Re = 50$, and the right side shows the shear stress profile for the case of $Re = 93$. The normalized shear stress, $\tau^* = \tau/\tau_0$, is defined as a ratio of the local shear stress $\tau = \mu_m \sqrt{2\mathbf{D} : \mathbf{D}}$ and the apparent shear stress $\tau_0 = \mu_m \Gamma$. In this study, for a given Ca condition, the same value of τ_0 is used

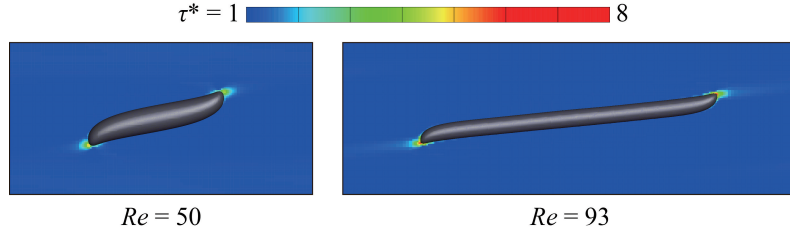


Figure 8: Normalized shear stress τ^* around a bubble for two Reynolds numbers under the condition of $Ca = 0.3$. The left image shows the shear stress profile at $Re = 50$ and the right image at $Re = 93$.

562 regardless of Re . For the case of $Re = 50$, the bubble reached a deformed stable
 563 state, and the shear stress profile around the bubble was drawn after the bubble
 564 attained a stable deformed state. As observed in previous sections, when the
 565 value of Re is slightly below the critical Re condition, the bubble does not settle
 566 into a deformed stable state. Instead, it alternates in an elongation and contrac-
 567 tion process. The shear stress profile for the case of $Re = 93$ was depicted when
 568 the bubble sufficiently elongated ($T = 14.9$). In comparison to the $Re = 50$ case
 569 on the left, the right image in Fig. 8 ($Re = 93$) shows a higher shear stress pro-
 570 file near the bubble endpoints as it undergoes an elongation state in the process
 571 toward breakup. The value of the maximum shear stress for the case of $Re = 50$
 572 is $\tau^* \approx 6$ and the maximum shear stress for the case of $Re = 93$ at the moment
 573 shown in Fig. 8 has the value of $\tau^* \approx 8$. The shear stress profile in Fig. 8 (color
 574 contour) is drawn in the range from $\tau^* = 1$ to $\tau^* = 8$, but, for emphasis, shear
 575 stress regions with $\tau^* \geq 6$ are illustrated in red. As shown in the figure, the
 576 strongest shear stresses are concentrated on the ends of the bubble for both Re
 577 conditions. This indicates that the strong shear stresses acting on the ends of
 578 the bubble are responsible for much of the bubble stretching. It is important
 579 to note that the magnitude of the shear stress acting on the ends of the bubble
 580 for the case of $Re = 93$ is much larger than that for the case of $Re = 50$.

581 We also observed that the shear stress inside the bubble was very small
 582 relative to that of the matrix fluid due to the bubble's very small density and
 583 viscosity. Since the force of strong shear stresses acting on the ends of the bubble
 584 is difficult to transfer across the interface, a sufficiently large Re condition is
 585 required for large bubble deformations.

586 In summary, we discover that for the Reynolds number sufficiently below
 587 the critical value, a relatively quick, unsteady elongation period gives way to a
 588 steady state (with no break up). On the other hand, for the Reynolds number
 589 close to the critical Reynolds number, there is a prolonged, unsteady elongation
 590 period in which periodic motion is observed, and the deformation parameter D is
 591 close to one. The “vacillating” behavior cannot last forever; ultimately (perhaps
 592 stochastically!), the bubble will either settle down or break. Regardless of the
 593 outcome, this vacillating behavior will always occur near the critical Reynolds
 594 number. In other words, irrespective of the result, we claim, using the grid

595 resolution of $R/16$, that one is assured of being within 3 percent of the critical
 596 Reynolds number (see Figure 3). We hypothesize that there will always be
 597 “vacillating” behavior if one is sufficiently close to the critical Reynolds number.
 598 In other words, given an almost infinite supply of computational resources, as
 599 one hones in closer and closer to the critical Reynolds number, a “tug of war”
 600 will be observed between the surface tension force trying to pull the bubble
 601 together versus the wall driven shear stress trying to pull the bubble apart.

602 4.4. Velocity field outside and inside the breaking bubble

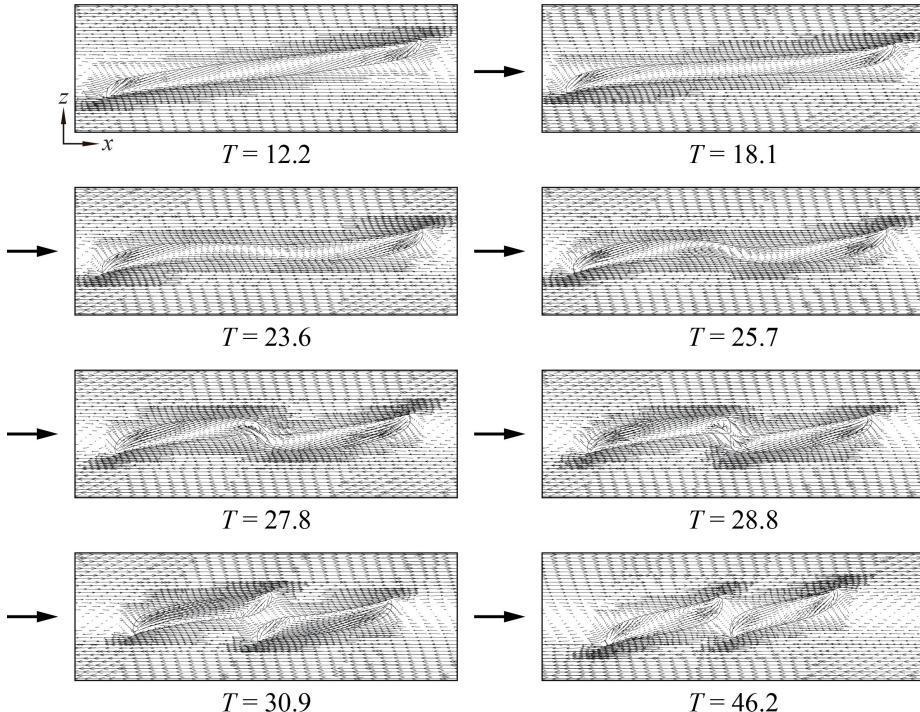


Figure 9: Fluid velocity field outside and inside the breaking bubble in shear flow at the condition $Ca = 0.3$ and $Re = 93$. The “bubble” critical Reynolds number corresponding to $Ca = 0.3$ is $92 < Re_c < 93$. ($\lambda = 1.2 \times 10^{-3}$, $\eta < 1.0 \times 10^{-3}$)

603 This section considers the fluid flow velocity field outside and inside the
 604 bubble during the shear-induced breakup process. Detailed velocity fields of
 605 the deforming and breaking drop have already been presented in a few references
 606 (Li et al. [33], Renardy and Cristini [47]). The behavior of the breakup process
 607 will influence the velocity fields for the drop and the bubble, so the velocity
 608 fields for the drop and the bubble are not similar. Figure 9 shows the velocity
 609 fields outside and inside the bubble at cross-sectional slices in the xz -plane
 610 for a flow condition of $Ca = 0.3$ and $Re = 93$. Regions around the bubble
 611 with a higher density of velocity vectors correspond to the level-1 grid portion

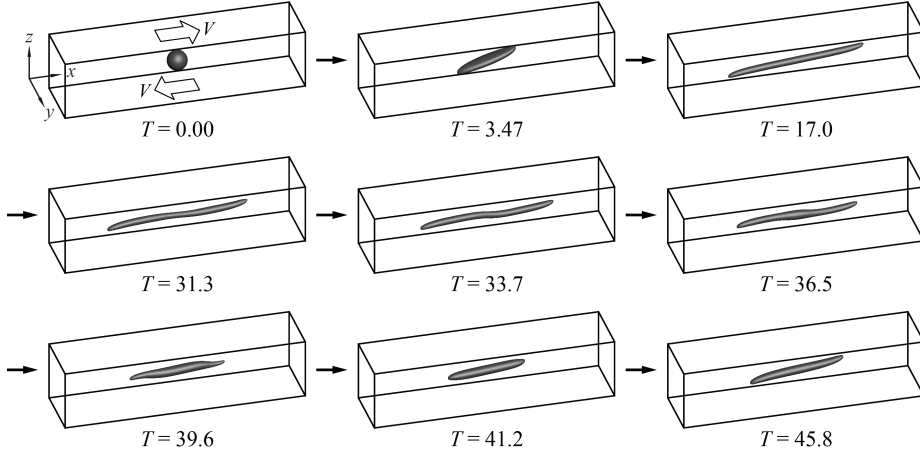


Figure 10: Time evolution of bubble deformation in shear flow at the condition of $Ca = 0.8$ and $Re = 42$. The “bubble” critical Reynolds number corresponding to $Ca = 0.8$ is $42 < Re_c < 43$. ($\lambda = 1.2 \times 10^{-3}$, $\eta < 1.0 \times 10^{-3}$)

of the AMR structure. The simulation results show that the velocity field inside the bubble is notably distinct from the surrounding flow field on the bubble’s exterior. The cross-sections at $T = 12.2$ and $T = 18.1$, taken during the elongation phase, show how shear forces at the lower and upper halves of the bubble act along the bottom and top surfaces, respectively, to deform the interface. Near the left and right edges of the bubble, inward interior flows (that point toward the bubble center) begin to develop. Strong shearing forces in the exterior near the bottom-left-end and top-right-end of the bubble interact with the interior flow field through the boundary to create cusped shapes at the bottom-left and top-right ends of the bubble. At the same time, the interface is laterally elongated in the x -direction. During the shrinking process, which occurs for $23.6 \leq T \leq 27.8$, inward flows within the bubble extend over a wider region and are no longer localized near the bubble edges. Then, we observe that circulating flows form at the thread-bridge part of the doglegged bubble shape over the time interval [25.7, 27.8]. During the breakup process ($T \sim 28.8$), higher-intensity inward flows are formed inside the bubble, near the pinch-off region, that are naturally larger than the surrounding interior flows and which are inextricably associated with the bubble migration illustrated in Figs. 6 and 7. As time proceeds further ($T = 46.2$), distinct inward flows are formed inside the daughter bubbles; the bubbles then migrate toward the side walls. For example, considering the left daughter bubble, we see that the mechanism responsible for this movement results from larger shear forces acting on the bottom-left end than those in the top-left end.

4.5. Effect of surface tension on bubble deformation and breakup

In previous sections, we considered numerical simulations of bubble deformation and breakup with a capillary number $Ca = 0.3$. In this section, we examine

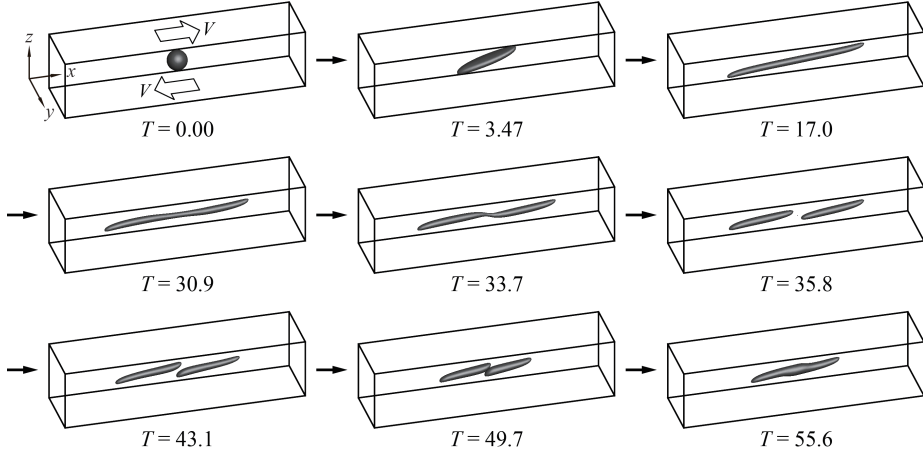


Figure 11: Time evolution of bubble deformation in shear flow at the condition of $Ca = 0.8$ and $Re = 43$. The “bubble” critical Reynolds number corresponding to $Ca = 0.8$ is $42 < Re_c < 43$. ($\lambda = 1.2 \times 10^{-3}$, $\eta < 1.0 \times 10^{-3}$)

the case of $Ca = 0.8$. We investigate the effect of interfacial tension on bubble deformation and breakup. Using $Ca = 0.8$ for both cases, Figures 10 and 11 present the time evolution of shear-induced bubble deformation and breakup with $Re = 42$ and $Re = 43$, respectively. We note that the bubble critical Reynolds number is around $Re_c \approx 43$, whereas $Re_c \approx 0$ for the corresponding case of the drop with $\lambda = \eta = 1$ (see e.g. Li et al. [33]). Note that Re_c for $Ca = 0.8$ is smaller than that for the condition of $Ca = 0.3$ since the bubble at $Ca = 0.8$ is more elastic due to the weaker effect of surface tension in this case. The results shown in Figs. 10 and 11 indicate that the bubble deformation and breakup process for the condition of $Ca = 0.8$ is analogous to that for $Ca = 0.3$. For the case of bubble deformation without breakup (Fig. 10), the bubble initially assumes a long elongated shape along the x -direction at around $T = 17.0$. The bubble then enters a compression stage over the time interval $[31.3, 41.2]$ and then elongates again at $T = 45.8$. On the other hand, for the case of bubble breakup (Fig. 11), an initial elongation phase is followed by a doglegged shape formation at $T = 33.7$. After that, the bubble ruptures from the thread-bridge part of the doglegged shape, producing two daughter bubbles ($T = 35.8$). The two daughter bubbles formed after the breakup move to the central area ($T = 49.7$) as in the case of $Ca = 0.8$ and $Re = 93$. Still, the two bubbles eventually coalesce in a region approximately centered in the computational domain ($T = 55.6$). We note that bubbles may coalesce after breaking up in a real experimental setting due to slight deviations in flow conditions and states. Although the process of bubble deformation and breakup for flow conditions with $Ca = 0.3$ and $Ca = 0.8$ are similar, a pronounced difference is that the bubble for $Ca = 0.8$ is more elongated and slender than that for $Ca = 0.3$ due to the smaller effect of surface tension for $Ca = 0.8$.

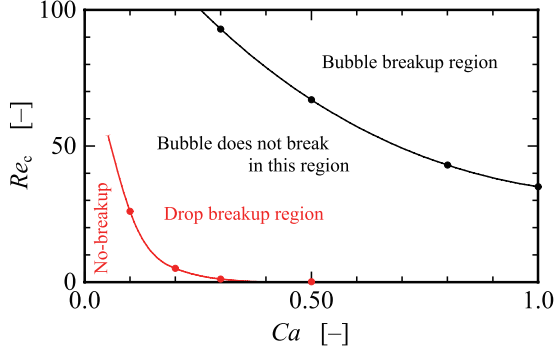


Figure 12: A plot of the critical Reynolds number versus capillary number for the data listed in Table 4. $\lambda = 1.2 \times 10^{-3}$, $\eta < 1.0 \times 10^{-3}$, $0.3 < Ca < 1$, and the initial/boundary conditions are given by (1). Given a new data point, (Ca, Re) , one can reliably predict whether the given (Ca, Re) pair will result in shear induced bubble break-up or not. Note, for the “Drop delineation curve,” $\lambda = \eta = 1$.

Table 4 lists, for representative Ca values, the corresponding critical Reynolds number, Re_c , for shear-induced bubble breakup. The data in Table 4 corresponds to $\lambda = 1.2 \times 10^{-3}$, $\eta < 1.0 \times 10^{-3}$, $0.3 < Ca < 1$, and the initial/boundary conditions are given by (1). The results in Table 4 indicate that sufficiently large shear forces are required for bubble breakup, even for large capillary numbers. In Figure 12 we plot the smooth interpolant of the data given in Table 4 and make the hypothesis that given a new data point, (Ca, Re) , shear-induced bubble break up will occur if the point (Ca, Re) is above the given critical curve, and the bubble will not break if the (Ca, Re) pair is below the critical curve. For comparison, a critical curve for the drop with $\lambda = \eta = 1$ is also indicated in Fig. 12. Including breakup and no-breakup critical curves for both the drop and the bubble will facilitate future identification of Re_c numbers and, thus, a complete general critical curve for a wide range of Ca numbers.

Table 4: Shear-induced bubble breakup for various flow conditions described in terms of column pairs of critical Reynolds numbers and corresponding capillary numbers. ($\lambda = 1.2 \times 10^{-3}$, $\eta < 1.0 \times 10^{-3}$)

Capillary number Ca	0.3	0.5	0.8	1.0
Critical Reynolds number Re_c	93	67	43	35

5. Conclusions

The bubble deformation and breakup process in liquid due to a driving simple linear shear flow was explored numerically using the CLSVOF computational method. In this study, the critical Reynolds number Re_c , at which bubble breakup first occurs, was determined for several flow conditions, and the

682 differences between the morphology of bubble deformation and breakup were
683 compared with the analogous morphology of drop deformation and breakup.

684 The numerical results revealed significant differences between bubble de-
685 formation and breakup and the corresponding drop dynamics. For the case
686 of a bubble, it was discovered that much stronger shear flows are necessary
687 to induce interface breakup compared with a drop immersed in a similar flow
688 field. That is, a much larger Reynolds number flow is required to induce bubble
689 breakup. The steps leading to bubble breakup were similar throughout the Ca
690 number range considered in our computations: the bubble underwent a sim-
691 ilar breakup mechanism in which rupture occurred at a thread-bridge part that
692 followed a doglegged shape formation stage. For bubble deformation without
693 breakup, near Re_c , the bubble did not maintain a stable deformed shape, unlike
694 drop deformation near the critical Reynolds number. The bubble exhibited pro-
695 nounced underdamped behavior: the bubble oscillated between elongating and
696 shrinking motions for non-rupturing flow conditions. At the same time, bubble
697 deformation under smaller Re conditions ($< Re_c$) led to a stable state. Com-
698 pared with the drop, we attribute the significant differences in morphology for
699 the bubble undergoing breakup to the density and viscosity ratio. Due to the
700 bubble's very small density and viscosity, it is comparatively difficult to transfer
701 the shear stresses acting on the ends of the bubble across the interface.

702 There are several directions for future work. In the present work, we varied
703 the capillary number and Reynolds number to study bubble deformation and
704 breakup morphology in the presence of a simple shear flow. For the future,
705 one can also vary (i) the viscosity ratio, (ii) the effect of the initial shape of
706 the bubble[39], (iii) the magnitude and direction of the gravitational force, (iv)
707 the non-Newtonian properties of the “matrix” liquid, (v) bubble deformation
708 and breakup due to a shear flow in a T junction[16], (vi) bubble deformation
709 and breakup confined shear flow (see [18] for the drop case), and (vii) bubble
710 deformation and breakup due to non-uniform shear flow (see [6] for the drop
711 case).

712 References

- 713 [1] Amani, A., Balcázar, N., Castro, J., Oliva, A., 2019. Numerical study of droplet deformation in shear flow using a con-
714 servative level-set method. Chemical Engineering Science 207,
715 153–171. URL: <http://www.sciencedirect.com/science/article/pii/S0009250919305123>, doi:<https://doi.org/10.1016/j.ces.2019.06.014>.
- 716 [2] Arienti, M., Li, X., Soteriou, M., Eckett, C., Sussman, M., Jensen, R., 2013. Coupled level-set/volume-of-fluid method for simulation of injector
717 atomization. Journal of propulsion and power 29, 147–157.
- 718 [3] Bazhlekov, I.B., Anderson, P.D., Meijer, H.E., 2006. Numerical investi-
719 gation of the effect of insoluble surfactants on drop deformation and

- 724 breakup in simple shear flow. *Journal of Colloid and Interface Science* 298, 369 – 394. URL: <http://www.sciencedirect.com/science/article/pii/S0021979705012658>, doi:<http://dx.doi.org/10.1016/j.jcis.2005.12.017>.
- 728 [4] Bento, D., Rodrigues, R.O., Faustino, V., Pinho, D., Fernandes, C.S.,
 729 Pereira, A.I., Garcia, V., Miranda, J.M., Lima, R., 2018. Deformation
 730 of red blood cells, air bubbles, and droplets in microfluidic devices:
 731 Flow visualizations and measurements. *Micromachines* 9, 151. URL:
 732 <https://www.mdpi.com/2072-666X/9/4/151>, doi:10.3390/mi9040151.
- 733 [5] Canedo, E.L., Favelukis, M., Tadmor, Z., Talmon, Y., 1993.
 734 An experimental study of bubble deformation in viscous liquids in simple shear flow. *AIChE Journal* 39, 553–559. URL:
 735 <https://aiche.onlinelibrary.wiley.com/doi/abs/10.1002/aic.690390403>,
 736 doi:<https://doi.org/10.1002/aic.690390403>,
 737 arXiv:<https://aiche.onlinelibrary.wiley.com/doi/pdf/10.1002/aic.690390403>.
- 738 [6] Chin, H.B., Han, C.D., 1980. Studies on droplet deformation and breakup. ii. breakup of a droplet in nonuniform shear flow. *Journal of rheology* 24, 1–37.
- 742 [7] Chu, P., Finch, J., Bournival, G., Ata, S., Hamlett, C., Pugh, R.J.,
 743 2019. A review of bubble break-up. *Advances in Colloid and Interface Science* 270, 108–122. URL: <https://www.sciencedirect.com/science/article/pii/S0001868619300211>, doi:<https://doi.org/10.1016/j.jcis.2019.05.010>.
- 747 [8] Cristini, V., Bławzdziewicz, J., Loewenberg, M., 2001. An adaptive
 748 mesh algorithm for evolving surfaces: simulations of drop breakup
 749 and coalescence. *Journal of Computational Physics* 168, 445 –
 750 463. URL: <http://www.sciencedirect.com/science/article/pii/S0021999101967130>, doi:<http://dx.doi.org/10.1006/jcph.2001.6713>.
- 752 [9] Cristini, V., Guido, S., Alfani, A., Bławzdziewicz, J., Loewenberg, M.,
 753 2003. Drop breakup and fragment size distribution in shear flow. *Journal
 754 of Rheology* 47, 1283–1298. URL: <http://scitation.aip.org/content/sor/journal/jor2/47/5/10.1122/1.1603240>, doi:<http://dx.doi.org/10.1122/1.1603240>.
- 758 [10] Croce, R., Griebel, M., Schweitzer, M.A., 2010. Numerical simulation of
 759 bubble and droplet deformation by a level set approach with surface tension
 760 in three dimensions. *International Journal for Numerical Methods in Fluids*
 761 62, 963–993. URL: <http://dx.doi.org/10.1002/fld.2051>, doi:10.1002/fld.2051.
- 765 [11] Drenckhan, W., Saint-Jalmes, A., 2015. The science of foaming. *Advances
 766 in Colloid and Interface Science* 222, 228–259. URL: <https://www.sciencedirect.com/science/article/pii/S0001868615000603>,

- 765 doi:<https://doi.org/10.1016/j.cis.2015.04.001>. reinhard Miller,
766 Honorary Issue.
- 767 [12] Eftekhari, M., Schwarzenberger, K., Heitkam, S., Eckert, K.,
768 2021a. Interfacial flow of a surfactant-laden interface under asym-
769 metric shear flow. *Journal of Colloid and Interface Science* 599,
770 837–848. URL: <https://www.sciencedirect.com/science/article/pii/S0021979721006457>, doi:<https://doi.org/10.1016/j.jcis.2021.04.126>.
- 771 [13] Eftekhari, M., Schwarzenberger, K., Heitkam, S., Javadi, A.,
772 Bashkatov, A., Ata, S., Eckert, K., 2021b. Interfacial be-
773 havior of particle-laden bubbles under asymmetric shear flow.
774 *Langmuir* 37, 13244–13254. URL: <https://doi.org/10.1021/acs.langmuir.1c01814>,
775 doi:10.1021/acs.langmuir.1c01814, arXiv:<https://doi.org/10.1021/acs.langmuir.1c01814>. pMID:
776 34726918.
- 777 [14] Ervin, E., Tryggvason, G., 1997. The rise of bubbles in a vertical shear
778 flow. *Journal of Fluids Engineering* 119(2), 443–449.
- 779 [15] Fang, Z., Shuai, Y., Huang, Z., Wang, J., Yang, Y., 2024. Inten-
780 sification of polyethylene devolatilization in twin-screw extruder
781 with additives. *Polymer Engineering & Science* 64, 2961–2974.
782 URL: <https://4sceppublications.onlinelibrary.wiley.com/doi/abs/10.1002/pen.26738>, doi:<https://doi.org/10.1002/pen.26738>, arXiv:<https://4sceppublications.onlinelibrary.wiley.com/doi/pdf/10.1002/pen.26738>.
- 783 [16] Frense, E., Rüdiger, F., Fröhlich, J., 2024. Modeling of dynamic bub-
784 ble deformation and breakup in t-junction channel flow. *Chemical En-
785 gineering Science* 300, 120579. URL: <https://www.sciencedirect.com/science/article/pii/S0009250924008790>, doi:<https://doi.org/10.1016/j.ces.2024.120579>.
- 786 [17] Gao, S., Shi, Y., Pan, G., Quan, X., 2022. Research on the
787 effect of asymmetric bubbles on the load characteristics of projec-
788 tiles during an underwater salvo. *Applied Ocean Research* 124,
789 103212. URL: <https://www.sciencedirect.com/science/article/pii/S0141118722001535>, doi:<https://doi.org/10.1016/j.apor.2022.103212>.
- 790 [18] Gupta, A., Sbragaglia, M., 2014. Deformation and breakup of viscoelastic
791 droplets in confined shear flow. *Physical Review E* 90, 023305.
- 792 [19] Hernandez, F.H., Rangel, R.H., 2017. Breakup of drops in simple
793 shear flows with high-confinement geometry. *Computers & Fluids* 146,
794 23 – 41. URL: <http://www.sciencedirect.com/science/article/pii/S0045793017300038>, doi:<https://doi.org/10.1016/j.compfluid.2017.01.001>.

- 806 [20] Hirt, C., Nichols, B., 1981. Volume of fluid (vof) method
 807 for the dynamics of free boundaries. Journal of Computational
 808 Physics 39, 201 – 225. URL: <http://www.sciencedirect.com/science/article/pii/0021999181901455>, doi:[http://dx.doi.org/10.1016/0021-9991\(81\)90145-5](http://dx.doi.org/10.1016/0021-9991(81)90145-5).
- 811 [21] Hoyt, N.C., 2013. The performance of passive cyclonic separators in mi-
 812 crogravity. Case Western Reserve University.
- 813 [22] Inamuro, T., 2006. Lattice boltzmann methods for viscous fluid flows and
 814 for two-phase fluid flows. Fluid Dynamics Research 38, 641. URL: <http://stacks.iop.org/1873-7005/38/i=9/a=A04>.
- 816 [23] Inamuro, T., Tomita, R., Ogino, F., 2003. Lattice boltzmann simu-
 817 lations of drop deformation and breakup in simple shear flows. Interna-
 818 tional Journal of Modern Physics B 17, 21–26. URL: <http://www.worldscientific.com/doi/abs/10.1142/S0217979203017035>, doi:10.
 819 1142/S0217979203017035.
- 821 [24] Ioannou, N., Liu, H., Zhang, Y., 2016. Droplet dynamics
 822 in confinement. Journal of Computational Science 17, 463 –
 823 474. URL: <http://www.sciencedirect.com/science/article/pii/S1877750316300308>, doi:<https://doi.org/10.1016/j.jocs.2016.03.009>. discrete Simulation of Fluid Dynamics 2015.
- 826 [25] Janssen, P., Anderson, P., 2008. A boundary-integral model for
 827 drop deformation between two parallel plates with non-unit viscosity
 828 ratio drops. Journal of Computational Physics 227, 8807–
 829 8819. URL: <http://www.sciencedirect.com/science/article/pii/S002199910800346X>, doi:<http://dx.doi.org/10.1016/j.jcp.2008.06.027>.
- 832 [26] Janssen, P.J.A., Anderson, P.D., 2007. Boundary-integral method
 833 for drop deformation between parallel plates. Physics of Fluids
 834 19. URL: <http://scitation.aip.org/content/aip/journal/pof2/19/4/10.1063/1.2715621>, doi:<http://dx.doi.org/10.1063/1.2715621>.
- 836 [27] Kang, M., Fedkiw, R.P., Liu, X.D., 2000. A boundary condition capturing
 837 method for multiphase incompressible flow. Journal of scientific computing
 838 15, 323–360.
- 839 [28] Khismatullin, D.B., Renardy, Y., Cristini, V., 2003. Inertia-induced
 840 breakup of highly viscous drops subjected to simple shear. Physics of Fluids
 841 15, 1351–1354. doi:<http://dx.doi.org/10.1063/1.1564825>.
- 842 [29] Komrakova, A., Shardt, O., Eskin, D., Derksen, J., 2014. Lattice
 843 boltzmann simulations of drop deformation and breakup in shear flow.
 844 International Journal of Multiphase Flow 59, 24 – 43. URL: <http://www.sciencedirect.com/science/article/pii/S0301932213001547>,
 845 doi:<http://dx.doi.org/10.1016/j.ijmultiphaseflow.2013.10.009>.

- 847 [30] Komrakova, A., Shardt, O., Eskin, D., Derksen, J., 2015. Effects
848 of dispersed phase viscosity on drop deformation and breakup
849 in inertial shear flow. *Chemical Engineering Science* 126, 150 –
850 159. URL: <http://www.sciencedirect.com/science/article/pii/S000925091400726X>, doi:<https://doi.org/10.1016/j.ces.2014.12.012>.
- 853 [31] Legendre, D., Magnaudet, J., 1998. The lift force on a spherical bubble in
854 a viscous linear shear flow. *Journal of Fluid Mechanics* 368, 81–126.
- 855 [32] Lewin-Jones, P., Lockerby, D.A., Sprittles, J.E., 2024. Collision of liquid
856 drops: bounce or merge? *Journal of Fluid Mechanics* 995, A1. doi:10.
857 1017/jfm.2024.722.
- 858 [33] Li, J., Renardy, Y., Renardy, M., 2000. Numerical simulation of
859 breakup of a viscous drop in simple shear flow through a volume-of-fluid
860 method. *Physics of Fluids* 12, 269–282. URL: <http://scitation.aip.org/content/aip/journal/pof2/12/2/10.1063/1.870305>, doi:<https://doi.org/10.1063/1.870305>.
- 863 [34] Li, X., Soteriou, M.C., 2016. High fidelity simulation and analysis of liq-
864 uid jet atomization in a gaseous crossflow at intermediate weber numbers.
865 *Physics of Fluids* 28.
- 866 [35] Lohse, D., 2018. Bubble puzzles: from fundamentals to applications. *Physical review fluids* 3, 110504.
- 868 [36] Müller-Fischer, N., Tobler, P., Dressler, M., Fischer, P., Windhab, E.J.,
869 2008. Single bubble deformation and breakup in simple shear flow. *Experi-
870 ments in fluids* 45, 917–926.
- 871 [37] Ohta, M., Akama, Y., Yoshida, Y., Sussman, M., 2014. Influence of the
872 viscosity ratio on drop dynamics and breakup for a drop rising in an im-
873 miscible low-viscosity liquid. *Journal of Fluid Mechanics* 752, 383–409.
874 doi:10.1017/jfm.2014.339.
- 875 [38] Ohta, M., Furukawa, T., Yoshida, Y., Sussman, M., 2019. A
876 three-dimensional numerical study on the dynamics and deformation
877 of a bubble rising in a hybrid carreau and fene-cr modeled poly-
878 mERIC liquid. *Journal of Non-Newtonian Fluid Mechanics* 265, 66–
879 78. URL: <https://www.sciencedirect.com/science/article/pii/S0377025718301952>, doi:<https://doi.org/10.1016/j.jnnfm.2018.12.012>.
- 882 [39] Ohta, M., Imura, T., Yoshida, Y., Sussman, M., 2005. A computational
883 study of the effect of initial bubble conditions on the motion of a gas bubble
884 rising in viscous liquids. *International journal of multiphase flow* 31, 223–
885 237.

- 886 [40] Ohta, M., Kikuchi, D., Yoshida, Y., Sussman, M., 2011. Robust numerical
 887 analysis of the dynamic bubble formation process in a viscous liquid.
 888 International Journal of Multiphase Flow 37, 1059–1071.
- 889 [41] Ohta, M., Sussman, M., 2012. The buoyancy-driven motion
 890 of a single skirted bubble or drop rising through
 891 a viscous liquid. Physics of Fluids 24, 112101. URL:
 892 <https://doi.org/10.1063/1.4765669>, doi:10.1063/1.4765669,
 893 arXiv:https://pubs.aip.org/aip/pof/article-pdf/doi/10.1063/1.4765669/14128560/112101_1.pdf
- 894 [42] Ohta, M., Yamaguchi, S., Yoshida, Y., Sussman, M., 2010. The sensitivity
 895 of drop motion due to the density and viscosity ratio. Physics of Fluids 22,
- 896 [43] Rallison, J.M., 1984. The deformation of small viscous drops
 897 and bubbles in shear flows. Annual Review of Fluid Mechanics 16, 45–66. URL: <http://dx.doi.org/10.1146/annurev.fl.16.010184.000401>,
 898 doi:10.1146/annurev.fl.16.010184.000401,
 899 arXiv:<http://dx.doi.org/10.1146/annurev.fl.16.010184.000401>.
- 900 [44] Renardy, Y., 2006. Numerical simulation of a drop undergoing large amplitude oscillatory shear. Rheologica acta 45, 223–227.
- 901 [45] Renardy, Y., 2007. The effects of confinement and inertia on the production
 902 of droplets. Rheologica Acta 46, 521–529. URL: <http://dx.doi.org/10.1007/s00397-006-0150-y>, doi:10.1007/s00397-006-0150-y.
- 903 [46] Renardy, Y., 2008. Effect of startup conditions on drop breakup under
 904 shear with inertia. International Journal of Multiphase Flow 34, 1185 – 1189. URL: <http://www.sciencedirect.com/science/article/pii/S030193220800089X>, doi:<http://dx.doi.org/10.1016/j.ijmultiphaseflow.2008.04.004>.
- 905 [47] Renardy, Y., Cristini, V., 2001a. Effect of inertia on drop breakup under
 906 shear. Physics of Fluids 13, 7–13. URL: <http://scitation.aip.org/content/aip/journal/pof2/13/1/10.1063/1.1331321>, doi:<http://dx.doi.org/10.1063/1.1331321>.
- 907 [48] Renardy, Y., Cristini, V., Li, J., 2002. Drop fragment distributions under
 908 shear with inertia. International Journal of Multiphase Flow 28, 1125 – 1147. URL: <http://www.sciencedirect.com/science/article/pii/S0301932202000228>, doi:[http://dx.doi.org/10.1016/S0301-9322\(02\)00022-8](http://dx.doi.org/10.1016/S0301-9322(02)00022-8).
- 909 [49] Renardy, Y.Y., Cristini, V., 2001b. Scalings for fragments produced
 910 from drop breakup in shear flow with inertia. Physics of Fluids 13,
 911 2161–2164. URL: <https://doi.org/10.1063/1.1384469>, doi:10.1063/
 912 1.1384469, arXiv:<https://doi.org/10.1063/1.1384469>.

- 924 [50] Rust, A., Manga, M., 2002. Bubble shapes and orientations in low re
925 simple shear flow. *Journal of Colloid and Interface Science* 249, 476–
926 480. URL: <https://www.sciencedirect.com/science/article/pii/S0021979702982925>, doi:<https://doi.org/10.1006/jcis.2002.8292>.
- 928 [51] Sanogo, B., Souidi, K., Marcatti, A., Vial, C., 2023. Food aeration: Ef
929 fect of the surface-active agent type on bubble deformation and break-up
930 in a viscous newtonian fluid: From single bubble to process-scale. *Food*
931 *Research International* 165, 112478. URL: <https://www.sciencedirect.com/science/article/pii/S0963996923000236>, doi:<https://doi.org/10.1016/j.foodres.2023.112478>.
- 934 [52] Schlüter, M., Herres-Pawlis, S., Nieken, U., Tuttlies, U., Bothe, D., 2021. Small-scale phenomena in reactive bubbly flows: Experiments, numerical
935 modeling, and applications. *Annual review of chemical and biomolecular
936 engineering* 12, 625–643.
- 938 [53] Sharifi, R., Varmazyar, M., Mohammadi, A., 2024. Investigating droplet and bubble deformation under shear flow using the multi-pseudo-potential scheme of lattice boltzmann method. *Advances in Applied Mathematics and Mechanics* 16, 519–548. URL: <https://global-sci.com/article/72820/investigating-droplet-and-bubble-deformation-under-shear-flow-using-the-multi-pseudo-potential-scheme-of-lattice-boltzmann-method>, doi:<https://doi.org/10.4208/aamm.OA-2021-0326>.
- 945 [54] Sines, J.N., Straiton, B.J., Zuccarelli, C.E., Marashdeh, Q.M., Teixeira, F.L., Fan, L.S., Motil, B.J., 2020. Study of gas-water flow inside
946 of a horizontal passive cyclonic gas-liquid phase separator system using
947 displacement-current phase tomography. *Gravitational and Space Research*
948 6, 28–43.
- 950 [55] Stewart, P., Lay, N., Sussman, M., Ohta, M., 2008. An improved sharp
951 interface method for viscoelastic and viscous two-phase flows. *Journal of
952 Scientific Computing* 35, 43–61.
- 953 [56] Stone, H.A., 1994. Dynamics of drop deformation and breakup
954 in viscous fluids. *Annual Review of Fluid Mechanics* 26,
955 65–102. URL: <http://dx.doi.org/10.1146/annurev.fl.26.010194.000433>,
956 doi:[10.1146/annurev.fl.26.010194.000433](https://doi.org/10.1146/annurev.fl.26.010194.000433),
957 arXiv:<http://dx.doi.org/10.1146/annurev.fl.26.010194.000433>.
- 958 [57] Sussman, M., 2003. A second order coupled level set and volume-
959 of-fluid method for computing growth and collapse of vapor bubbles. *Journal of Computational Physics* 187, 110–136. URL: <https://www.sciencedirect.com/science/article/pii/S0021999103000871>,
960 doi:[https://doi.org/10.1016/S0021-9991\(03\)00087-1](https://doi.org/10.1016/S0021-9991(03)00087-1).

- 963 [58] Sussman, M., Almgren, A.S., Bell, J.B., Colella, P., Howell, L.H.,
 964 Welcome, M.L., 1999. An adaptive level set approach for incom-
 965 pressible two-phase flows. *Journal of Computational Physics* 148, 81
 966 – 124. URL: <http://www.sciencedirect.com/science/article/pii/S002199919896106X>, doi:<https://doi.org/10.1006/jcph.1998.6106>.
- 968 [59] Sussman, M., Puckett, E.G., 2000. A coupled level set and
 969 volume-of-fluid method for computing 3d and axisymmetric incompress-
 970ible two-phase flows. *Journal of Computational Physics* 162, 301–
 971 337. URL: <http://www.sciencedirect.com/science/article/pii/S0021999100965379>, doi:<https://dx.doi.org/10.1006/jcph.2000.6537>.
- 973 [60] Sussman, M., Smereka, P., Osher, S., 1994. A level set ap-
 974 proach for computing solutions to incompressible two-phase flow.
 975 *Journal of Computational Physics* 114, 146 – 159. URL: <http://www.sciencedirect.com/science/article/pii/S0021999184711557>,
 976 doi:<http://dx.doi.org/10.1006/jcph.1994.1155>.
- 978 [61] Sussman, M., Smith, K., Hussaini, M., Ohta, M., Zhi-Wei, R., 2007. A
 979 sharp interface method for incompressible two-phase flows. *Journal of Com-
 980 putational Physics* 221, 469–505. URL: <https://www.sciencedirect.com/science/article/pii/S0021999106002981>, doi:<https://doi.org/10.1016/j.jcp.2006.06.020>.
- 983 [62] Tanguy, S., Ménard, T., Berlemont, A., 2007. A level set method for
 984 vaporizing two-phase flows. *Journal of Computational Physics* 221, 837–
 985 853.
- 986 [63] Tatebe, O., 1993. The multigrid preconditioned conjugate gradient method,
 987 in: NASA. Langley Research Center, The Sixth Copper Mountain Confer-
 988 ence on Multigrid Methods, Part 2.
- 989 [64] Taylor, G.I., 1932. The viscosity of a fluid containing small drops of another
 990 fluid. *Proceedings of the Royal Society of London A: Mathematical, Phys-
 991 ical and Engineering Sciences* 138, 41–48. doi:[10.1098/rspa.1932.0169](https://doi.org/10.1098/rspa.1932.0169).
- 992 [65] Taylor, G.I., 1934. The formation of emulsions in definable fields of flow.
 993 *Proceedings of the Royal Society of London A: Mathematical, Physical and
 994 Engineering Sciences* 146, 501–523. doi:[10.1098/rspa.1934.0169](https://doi.org/10.1098/rspa.1934.0169).
- 995 [66] Unverdi, S.O., Tryggvason, G., 1992. A front-tracking method
 996 for viscous, incompressible, multi-fluid flows. *Journal of Computa-
 997 tional Physics* 100, 25 – 37. URL: <http://www.sciencedirect.com/science/article/pii/002199919290307K>, doi:[https://dx.doi.org/10.1016/0021-9991\(92\)90307-K](https://dx.doi.org/10.1016/0021-9991(92)90307-K).
- 1000 [67] Wang, A., Evans, G., Mitra, S., 2023. A review of bub-
 1001 ble surface loading and its effect on bubble dynamics. *Miner-
 1002 als Engineering* 199, 108105. URL: <https://www.sciencedirect.com/science/article/pii/S002199912300050X>, doi:<https://doi.org/10.1016/j.men.2023.108105>.

- 1003 com/science/article/pii/S089268752300119X, doi:<https://doi.org/10.1016/j.mineng.2023.108105>.
- 1005 [68] Wang, Z., Shi, D., Zhang, A., 2015. Three-dimensional lattice boltzmann simulation of bubble behavior in a flap-induced shear flow. Computers & Fluids 123, 44 – 53. URL: <http://www.sciencedirect.com/science/article/pii/S0045793015003199>, doi:<https://doi.org/10.1016/j.compfluid.2015.09.007>.
- 1010 [69] Wei, Y.K., Qian, Y., Xu, H., 2012. Lattice boltzmann simulations of single bubble deformation and breakup in a shear flow. The Journal of Computational Multiphase Flows 4, 111–117. URL: <https://doi.org/10.1260/1757-482X.4.1.111>, doi:10.1260/1757-482X.4.1.111, arXiv:<https://doi.org/10.1260/1757-482X.4.1.111>.
- 1015 [70] Wong, A., Park, C., 2012. A visualization system for observing plastic foaming processes under shear stress. Polymer Testing 31, 417–424. URL: <https://www.sciencedirect.com/science/article/pii/S0142941811002169>, doi:<https://doi.org/10.1016/j.polymertesting.2011.12.012>.
- 1020 [71] Yoshikawa, H.N., Zoueshtiagh, F., Caps, H., Kurowski, P., Petitjeans, P., 2010. Bubble splitting in oscillatory flows on ground and in reduced gravity. The European Physical Journal E 31, 191–199.
- 1023 [72] Zhang, J., Miksis, M.J., Bankoff, S.G., 2006. Nonlinear dynamics of a two-dimensional viscous drop under shear flow. Physics of Fluids 18. URL: <http://scitation.aip.org/content/aip/journal/pof2/18/7/10.1063/1.2222336>, doi:<http://dx.doi.org/10.1063/1.2222336>.
- 1027 [73] Zhang, J., Ni, M.J., Magnaudet, J., 2021a. Three-dimensional dynamics of a pair of deformable bubbles rising initially in line. part 1. moderately inertial regimes. Journal of Fluid Mechanics 920, A16.
- 1030 [74] Zhang, J., Ni, M.J., Magnaudet, J., 2022. Three-dimensional dynamics of a pair of deformable bubbles rising initially in line. part 2. highly inertial regimes. Journal of Fluid Mechanics 943, A10.
- 1033 [75] Zhang, J., Shu, S., Guan, X., Yang, N., 2021b. Regime mapping of multiple breakup of droplets in shear flow by phase-field lattice boltzmann simulation. Chemical Engineering Science 240, 116673. URL: <https://www.sciencedirect.com/science/article/pii/S0009250921002384>, doi:<https://doi.org/10.1016/j.ces.2021.116673>.
- 1039 [76] Zhang, W., Almgren, A., Beckner, V., Bell, J., Blaschke, J., Chan, C., Day, M., Friesen, B., Gott, K., Graves, D., Katz, M., Myers, A., Nguyen, T., Nonaka, A., Rosso, M., Williams, S., Zingale, M., 2019. AMReX: a framework for block-structured adaptive mesh refinement. Journal of Open

1043
1044

Source Software 4, 1370. URL: <https://doi.org/10.21105/joss.01370>,
doi:10.21105/joss.01370.